The Astrophysical Journal Letters, 933:L35 (19pp), 2022 July 10 https://doi.org/10.3847/2041-8213/ac75d7

A Detailed Temperature Map of the Archetypal Protostellar Shocks in L1157

S. Feng (冯思轶)[1], H. B. Liu[2], P. Caselli[3], A. Burkhardt[4], F. Du[5,6], R. Bachiller[7], C. Codella[8,9], and C. Ceccarelli[9]
[1] Department of Astronomy, Xiamen University, Zengcuo'an West Road, Xiamen, 361005, People's Republic of China; syfeng@xmu.edu.cn
[2] Academia Sinica Institute of Astronomy and Astrophysics, No.1, Sec. 4, Roosevelt Rd, Taipei 10617, Taiwan, Republic of China
[3] Max-Planck-Institut für extraterrestrische Physik, Gießenbachstraße 1, D-85748, Garching bei München, Germany
[4] Wellesley College, 106 Central Street, Wellesley, MA 02481, USA
[5] Purple Mountain Observatory and Key Laboratory of Radio Astronomy, Chinese Academy of Sciences, Nanjing 210033, People's Republic of China
[6] School of Astronomy and Space Science, University of Science and Technology of China, Hefei, Anhui 230026, People's Republic of China
[7] Observatorio Astronomico Nacional (OAN, IGN), Calle Alfonso XII, 3, E-28014 Madrid, Spain
[8] INAF-Osservatorio Astrofisico di Arcetri, Largo E. Fermi 5, I-50125, Florence, Italy
[9] Univ. Grenoble Alpes, CNRS, IPAG, F-38000 Grenoble, France
Received 2022 April 4; revised 2022 June 3; accepted 2022 June 3; published 2022 July 11

Abstract

We present sensitive NH_3 (1,1)–(7,7) line images from the Karl G. Jansky Very Large Array toward successive shocks, which are associated with the blueshifted outflow lobe driven by the compact protobinary system L1157. Within a projection distance of 0.1 pc, our observations not only trace the quiescent and cold gas in the flattened envelope, but also illustrate the complex physical and chemical processes that take place where the high-velocity jet impinges on its surrounding medium. Specifically, the NH_3 ortho-to-para ratio is enhanced by a factor of 2–2.5 along the jet path, where the velocity offset between the line peak and the blueshifted wing reaches values as high as $10\,km\,s^{-1}$; it also shows a strong spatial correlation with the NH_3 column density, which is enhanced to $>10^{16}\,cm^{-2}$ toward the shock cavities. At a linear resolution of 1500 au, our refined temperature map from the seven NH_3 lines shows a gradient from the warm B0 eastern cavity wall (>120 K) to the cool cavity B1 and the earlier shock B2 (<80 K), indicating shock heating.

Unified Astronomy Thesaurus concepts: Low mass stars (2050); Stellar bow shocks (1586); Astrochemistry (75)

1. Introduction

Protostellar shocks are commonly detected in the earliest stage of star formation. Generated by the impact of supersonic jets from the central protostars on their dense natal parental cloud (e.g., Frank et al. 2014), the shocks create a dense and warm environment in a short timescale by compressing and heating the surrounding gas. Such an environment speeds up chemical processes, which are infeasible in the preshock gas, including, but not limited to, endothermic chemical reactions, ice mantle vaporization, and sputtering (e.g., Viti et al. 2011).

The target region of this work is an archetypal region containing successive shocks (named B0, B1, and B2), which are associated with the blueshifted outflow lobe from the nearby ($d\sim352$ pc; Zucker et al. 2019) Class 0 compact protobinary system L1157-mm ($\simeq 3L_{\odot}$; Tobin et al. 2010, 2022). Kinematically, an episodic precessing jet driven by the protobinary system hits the shock cavity wall, generating bright knots (e.g., Gueth et al. 1996, 1998; Podio et al. 2016). Within a projection of 0.1 pc from the protobinary system in the plane of the sky, the kinematic age difference of these shock knots is ~1000 yr, so this region provides us with one of the best space laboratories to study the time-dependent shock chemistry (e.g., Lefloch et al. 2010; Codella et al. 2017).

Multiwavelength line surveys have intensively observed this region, especially B1, over the decades (e.g., Herschel-CHESS, Ceccarelli et al. 2010; IRAM 30 m-ASAI, Lefloch et al. 2018; NOrthern Extended Millimeter Array (NOEMA)-SOLIS, Ceccarelli et al. 2017) and revealed chemical complexities from diatomic molecules to complex organics (e.g., Tafalla & Bachiller 1995; Bachiller et al. 2001; Benedettini et al. 2007; Arce et al. 2008; Codella et al. 2009, 2010; Lefloch et al. 2012; Benedettini et al. 2013; Busquet et al. 2014; Podio et al. 2014; Fontani et al. 2014a; Codella et al. 2015, 2017; Lefloch et al. 2017, 2018; Codella et al. 2020; Feng et al. 2020; Spezzano et al. 2020). It is clear that sufficient observational data exist to carry out a systematic study of shock chemistry, i.e., examining the origin, excitation, and chemical complexity of different species. However, a crucial input for chemical modeling is the physical structure of this region, which is still missing.

Previous observations attempted to use several inversion lines of NH_3 at centimeter wavelengths to provide constraints on the kinetic temperature of this region, given that these lines have been widely used as an interstellar thermometer[10] for molecular gas with number density $n>10^4\,cm^{-3}$ (Ho & Townes 1983; Walmsley & Ungerechts 1983; Crapsi et al. 2007; Rosolowsky et al. 2008; Juvela & Ysard 2011; Caselli et al. 2017). However, hindered by the low spatial/velocity resolutions of single-dish point observations (e.g., Bachiller et al. 1993 observed the (1,1)–(4,4) lines; Umemoto et al. 1999 observed the (1,1)–(6,6) lines) and the insufficient sensitivity of interferometric observations (Tafalla & Bachiller 1995 observed only the (1,1)–(3,3) lines), several assumptions were

[10] The majority of the NH_3 population stays in the metastable levels $J=K$, where J is the total angular momentum quantum number of NH_3, and K is the projection of J on the rotational axis. The inversion transitions from different rotational ladders of NH_3 are coupled only collisionally. Having similar frequencies at 1.3 cm wavelength, several inversion lines of NH_3 can be observed simultaneously, so that the calibration uncertainties in the line ratio measurements are minimized.

made in their works, leading to large uncertainties in their conclusions.

Interferometric observations have been carried out recently, targeting line ladders of CH_3CN, H_2CO, CS, and molecular ions. Although these works provide constraints on the H_2 volume density n (e.g., Benedettini et al. 2013; Gómez-Ruiz et al. 2015) and molecular rotation temperature (e.g., Codella et al. 2009; Podio et al. 2014) toward several knots, these attempts are only toward B1.

In this paper, with the newest NH_3 (1,1)–(7,7) observations at high-spatial and high-velocity resolutions, we provide a detailed temperature map over B0–B1–B2 and discuss the complex physical and chemical processes that take place when the high-velocity jet impinges on its surrounding medium.

2. Observations and Data Reduction

Using the Karl G. Jansky Very Large Array (JVLA), we have performed observations toward L1157 B0–B1–B2 at the K band in D-array configurations from September to November in 2018. For all observations, a common phase center at $20^h39^m10^s.2$, $+68°01'10''.5$ (J2000) and a systemic velocity $V_{sys} \sim 2.7\,\mathrm{km\,s^{-1}}$ were adopted from the Herschel results on the o-NH_3 (1_0–0_0) line (Codella et al. 2010). Employing the three-bit sampler, our correlator setup uses 27 independent spectral windows to cover the NH_3 (1,1)–(7,7) transitions (with E_u/k_B ranges from 24 to 539 K) and broadband continuum simultaneously.

All epochs of observations used 1331+305 (3C 286), J1642+3948, and J2022+6136 for absolute flux, passband, and complex grain calibrations, respectively.

Following the standard strategy by using the Common Astronomy Software Applications (CASA; McMullin et al. 2007) package release 5.4.0, we manually calibrated the JVLA data. The absolute fluxes of the flux calibrator 3C 286 were referenced from the Perley–Butler 2017 standards (Perley & Butler 2017). For different epochs, a 10%–15% nominal absolute flux calibration accuracy may have to be assumed according to the official documentation.[11] Nevertheless, the absolute flux calibration errors are factored out when deriving spectral line ratios.

Using the CASA task TCLEAN in CASA 5.4.6, we performed the spectral line imaging (setting the specmode as "cube") and broadband continuum imaging (setting the specmode as "mfs") by applying the "multiscale" imaging option with scales values of 0, 5, and 15 times the pixel size. The primary beam (pb) and the maximum recoverable angular scales for the single pointing observations are $\sim$119″ and $\sim$61″ at 23.7 GHz, respectively. We test the Briggs robust weighting[12] r as 2.0, –2.0, and 0.5. The continuum shows $>4\sigma$ emission only toward the protobinary system, although this system is not resolved from our observations. The continuum intensity peak, measured at different weightings before and after pb correction, is 5σ–10σ, with 1σ rms varying in the range of 0.01–0.04 mJy beam^{-1}, which is consistent with Tobin et al. (2022). For all the targeted NH_3 lines, their image properties[13] are listed in Table 1.

[11] https://science.nrao.edu/facilities/vla/docs/manuals/oss/performance/fdscale

[12] The naturally weighted ($r = 2.0$) image has high sensitivity but low spatial resolution, the uniformly weighted ($r = -2.0$) image has low sensitivity but high spatial resolution, and the image with $r = 0.5$ is a good trade-off between resolution and sensitivity.

[13] Line image properties have negligible changes before and after continuum subtraction.

3. Results

3.1. Molecular Spatial Distribution

The hyperfine multiplets of NH_3 (1,1)–(7,7) cover a velocity offset from -30 to $+30\,\mathrm{km\,s^{-1}}$ with respect to the V_{sys} (e.g., Ho & Townes 1983; Mangum & Shirley 2015). We detected all the seven lines toward our target region, with their hyperfine multiplets partially resolvable at a velocity resolution of 0.05–0.2 km s^{-1} (Table 1).

Extracting their naturally weighted spectra toward different jet knots from B0 to B2 (Figure A1), we found that the satellite components of each line have a signal-to-noise ratio S/N > 3 in the velocity range of -25 to $+25\,\mathrm{km\,s^{-1}}$. Over this velocity range, the integrated intensities of all seven lines trace an extended structure (Figures 1 and B1)—from the rim of the B0 eastern cavity wall to two bow-shock cavities associated with B1 and B2 (denoted as C2 and C1, respectively, in Gueth et al. 1998).

Comparing the total fluxes of the (1,1)–(4,4) lines from our JVLA observations with those given by the single-dish observations (Bachiller et al. 1993; Umemoto et al. 1999)[14] we found 20% and 15% of the flux missing toward B1 and B2, respectively. Note that the angular resolution of Effelsberg observations (Bachiller et al. 1993) is coarser than that of JVLA by a factor of 10, so effects such as pointing errors and the attenuation at the edge of the Gaussian-shaped Effelsberg beam, may bring uncertainty in the comparison. Although we cannot precisely recover the flux per pixel from the Effelsberg single-point data, such comparison indicates that the images in this work cover the NH_3 extended emissions toward B1 and B2 at a similar level.

Limited by the largest recoverable angular scale with one pointing in these observations, only the central region (i.e., within the gray circle in Figure 1) of the image has high fidelity. In order to apply the kinetic temperature map derived from NH_3 lines to the chemical property measurements (i.e., column density, abundance) of the other molecular lines at a spatial resolution of $\sim$1500 au, we labeled seven clumpy substructures (B0e, B1a, B1b, B1c, B1f, B1i, and B2a), which were identified from previous observations (e.g., by using line emissions from CH_3CN, HCN, CH_3OH, SiO, CS, H_2CO, HCO^+, HNCO, SO, and SO_2 in Benedettini et al. 2007; Codella et al. 2009; Gómez-Ruiz et al. 2013; Burkhardt et al. 2016; Feng et al. 2020). Moreover, the large pb of JVLA allows us to investigate the complete B0 cavity wall and the B2 shock front together with the phase center B1. In the maps with pb correction (Figure B1), we found two clumpy structures showing stronger emissions than the rest of B0 and B2. Both structures are along the jet path derived by Podio et al. (2016) and were previously denoted B0a and B2b in Burkhardt et al. (2016).

Each substructure may be traced by more than one molecule, and the absolute coordinate of these intensity peaks (listed in Table A1) are different from tracer to tracer[15] by 1″–2″. Nevertheless, these nine clumpy substructures disentangled three chemical layers (e.g., Fontani et al. 2014b; Codella et al. 2017)

[14] The line emission peaks observed with Nobeyama 45 m (Umemoto et al. 1999) are in general lower than those observed with Effelsberg 100 m (Bachiller et al. 1993) by a factor of 1.5–2, probably due to the beam dilution.

[15] B2a corresponds to the emission peak of CO toward B2 in the present work, which is $\sim$5″ offset to the SO and SO_2 emission peak reported in Feng et al. (2020) and is $\sim$2″ offset to the coordinate reported in Burkhardt et al. (2016).

Table 1
Spectroscopic Parameter of the Targeted NH_3 Lines and Their Image Properties from the JVLA Observations

Mol.	Freq. (GHz)	Transition	$S\mu^2$[a] (D^2)	E_u/k_B[b] (K)	No. hfs[c]	ΔV[d] (km s^{-1})	$\Delta\theta$ (P.A.)[e] ($'' \times ''$,°)			1σ rms[f] (mJy $beam^{-1}$ ch^{-1})		
							$r = 2.0$	$r = 0.5$	$r = -2.0$	$r = 2.0$	$r = 0.5$	$r = -2.0$
p-NH_3	23.694	1(1)0a−1(1)0s	6.6	24	18[g]	0.049	4.″63 × 3.″77 (17°)	4.″24 × 3.″19 (26°)	3.″71 × 2.″63 (31°)	6.3	5.1	6.1
p-NH_3	23.723	2(2)0a−2(2)0s	14.7	65	21[g]	0.197	4.″90 × 3.″81 (19°)	4.″60 × 3.″36 (23°)	4.″34 × 2.″93 (29°)	2.2	2.5	2.3
o-NH_3	23.870	3(3)0a−3(3)0s	46.4	124	26[h]	0.196	4.″20 × 3.″60 (− 6°)	3.″67 × 3.″01 (2°)	3.″20 × 2.″46 (10°)	2.8	2.9	2.8
p-NH_3	24.139	4(4)0a−4(4)0s	31.8	201	7[h]	0.194	4.″12 × 3.″53 (− 1°)	3.″62 × 2.″97 (3°)	3.″15 × 2.″43 (10°)	1.3	1.3	2.2
p-NH_3	24.533	5(5)0a−5(5)0s	40.5	296	7[i]	0.191	4.″25 × 3.″65 (0°)	3.″74 × 3.″05 (10°)	3.″31 × 2.″48 (18°)	1.2	1.3	2.2
o-NH_3	25.056	6(6)0a−6(6)0s	98.5	409	7[i]	0.187	4.″50 × 3.″65 (20°)	4.″09 × 3.″10 (26°)	3.″62 × 2.″51 (28°)	1.3	1.3	2.3
p-NH_3	25.715	7(7)0a−7(7)0s	56.3	539	7[i]	0.182	4.″09 × 3.″46 (2°)	3.″61 × 2.″90 (8°)	3.″19 × 2.″34 (16°)	1.1	1.2	2.2

Notes.
[a] Sum of all hyperfine multiplets.
[b] Higher upper energy level of the transition.
[c] Number of hyperfine multiplets used for deriving the optical depth of the main component.
[d] Channel width.
[e] Synthesized beam.
[f] Without pb correction (with uniform noise level over the entire map), without angular resolution smoothing, measured with the referred beam size ("beam") per channel ("ch").
[g] Number of hyperfine multiplets, adopted from Mangum & Shirley (2015).
[h] Number of hyperfine multiplets, adopted from `PySpecKit` (Ginsburg & Mirocha 2011).
[i] Number of hyperfine multiplets, adopted from TopModel in "Splatalogue" database (https://www.cv.nrao.edu/php/splat).

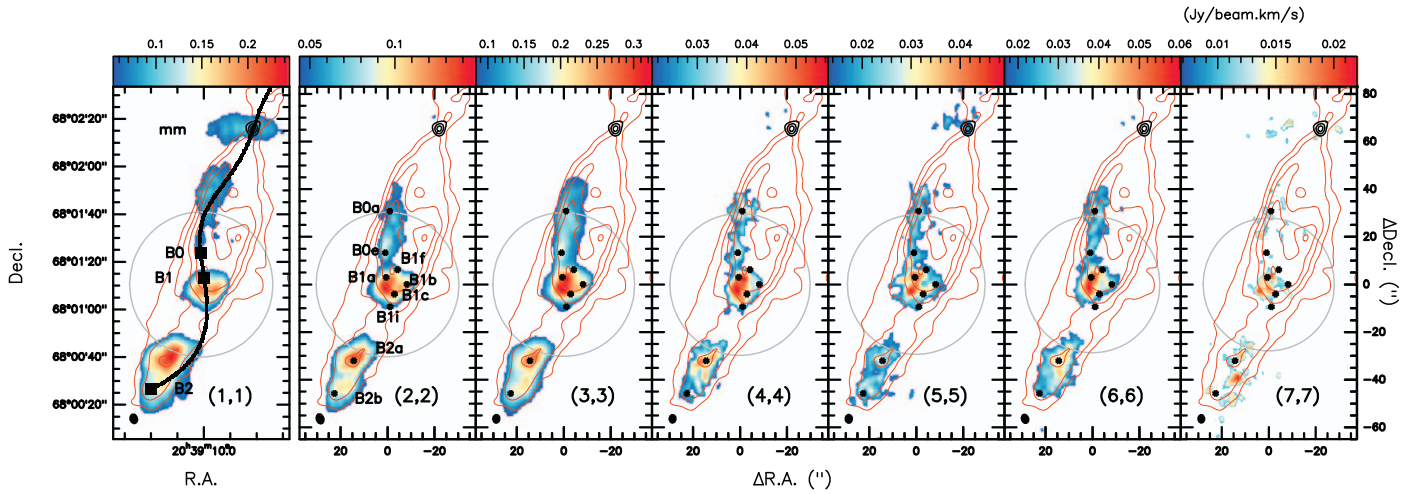

Figure 1. The outline of the southern (blueshifted) outflow lobe from the Class 0 compact protobinary system L1157-mm. Color maps show the naturally weighted ($r = 2.0$) intensity maps of NH_3 (1,1)–(7,7) integrated over the velocity range of -25 to $+25$ km s^{-1} (without pb correction). Line emissions with $<5\sigma$ rms are blank in each panel. The red contours, starting from 8σ ($\sigma = 0.27$ Jy beam^{-1}) and increasing with a step of 8σ, show the CO (1–0) emission, obtained from the NOEMA and IRAM-30 m combination (Gueth et al. 1996). The black contours, starting from 4σ ($\sigma = 0.01$ mJy beam^{-1}) and increasing with a step of 4σ, show the naturally weighted continuum emission at 1.3 mm (without pb correction). The gray circle in each panel indicates the largest recoverable scale at the corresponding line rest frequency, and the angular resolution is plotted at the bottom-left of each panel. In the panel of the (1,1) line, the black curve guides the path of the precessing jet from the driving source L1157-mm as modeled by Podio et al. (2016). The black squares indicate the shock knots B0, B1, and B2. In the panels of the (2,2)–(7,7) lines, nine clumpy substructures are labeled.

and marked down the kinematic history from B0 to B1–B2 shocks. For example, B0e, B1a, and B2b indicate the knots where episodic ejection impacts against the cavity wall (Gueth et al. 1998; Podio et al. 2016; Spezzano et al. 2020), B1a–B1c–B1b indicate the shock front, and B1i indicates the possible magnetic precursor (Gueth et al. 1998).

The field of view is sufficiently large to cover part of the flattened envelope surrounding the driving source denoted as mm. In the naturally weighted images without pb correction (Figure 1), lines have the same noise level over the entire map, only the (1,1) line shows $>3\sigma$ emission toward the flattened envelope. Applying the pb correction, the integrated intensities of all lines toward the phase center B1 are the same as before, but they increase toward B0, B2a, B2b, and mm by a factor of 1.2, 1.3, 1.7, and 4.2 respectively, and all line emissions reveal part of the flattened structure (Figure B1). Note that the region with $>5\sigma$ emissions on the (2,2)–(7,7) images is $\sim 10''$ north of the flattened structure, a relatively larger portion of which is revealed by the (1,1) map. The shift for the higher NH_3 transitions may be a temperature effect (e.g., the northern warmer portion may be slightly tilted and closer to the heating source). Because this region is at the edge of our pb, it is also likely to be contaminated by the sidelobe fringe pattern, and its missing flux cannot be estimated. The uniformly weighted images should have less sidelobe effect toward the pb edge, but the worse sensitivity there makes this structure quite diffuse (see Figure B1). In the following analysis, we use the naturally weighted images for better sensitivity.

3.2. Velocity Structure

The integrated intensity map projects the molecular line distribution in the 2D plane of the sky, but it misses the velocity information in the line of sight. Our source contains two successive shocks, as well as an entrained processing jet, which is associated with an outflow. Characterizing the velocity structure resulting in such complicated kinematics is not straightforward. Pixel by pixel, we measure two characteristic velocities: V_p, where the line intensity peaks, and V_b, where the line intensity of the blueshifted wing goes down to zero.

Traditionally, the peak velocity V_p toward each pixel can be shown as the "first-moment" (the intensity-weighted average velocity) map or the centroid velocity map provided by the hyperfine multiplets fit to a particular line. Because of the shocks, all spectra observed toward our target show deviations from a Gaussian profile (Figure A1). Therefore, neither map can provide a reliable gradient of V_p over the entire region. Instead, we apply the "ninth-moment" algorithm implemented by CASA and obtain a V_p map smoother than the "first-moment" map and the centroid velocity map. Similar image quality is also achieved when we test the `bettermoments` code[16] (Teague & Foreman-Mackey 2018) to fit a quadratic model to the pixel of maximum intensity and its two neighboring pixels.

For the spectrum of each pixel, starting from the intensity peak, we modify the "eleventh moment" algorithm[17] implemented by CASA, search blueward to find the first velocity channel (within -10 km s^{-1} to 5 km s^{-1}) V_b, where the intensity becomes equal to or less than zero.

We present the V_p ("ninth moment") and V_b ("eleventh moment") maps of one para (p-, $K \neq 3n$) NH_3 line (2,2) and one ortho (o-, $K = 3n$) NH_3 line (3,3) throughout B0–B1–B2 in Figure 2. These lines were selected because they are observed at a relatively high-velocity resolution (0.197 km s^{-1}) and show higher S/Ns than the other lines toward the entire region. From the V_p maps of both lines, their intensities peak at around the V_{sys} (2–3 km s^{-1}) toward the cavity wall along B0a–B0e–B1a–B2a, while the peaks are blueshifted to 0–1 km s^{-1} toward the west of the bow shock B1f–B1b–B1i. The V_b maps indicate that the blueshifted wings of both lines extend to -3 km s^{-1} toward B2a, -5 km s^{-1} toward B2b, and further down to -9 km s^{-1} toward B0 and B1. A lower radial velocity downstream may be a

[16] https://github.com/richteague/bettermoments
[17] https://casa.nrao.edu/docs/casaref/image.moments.html

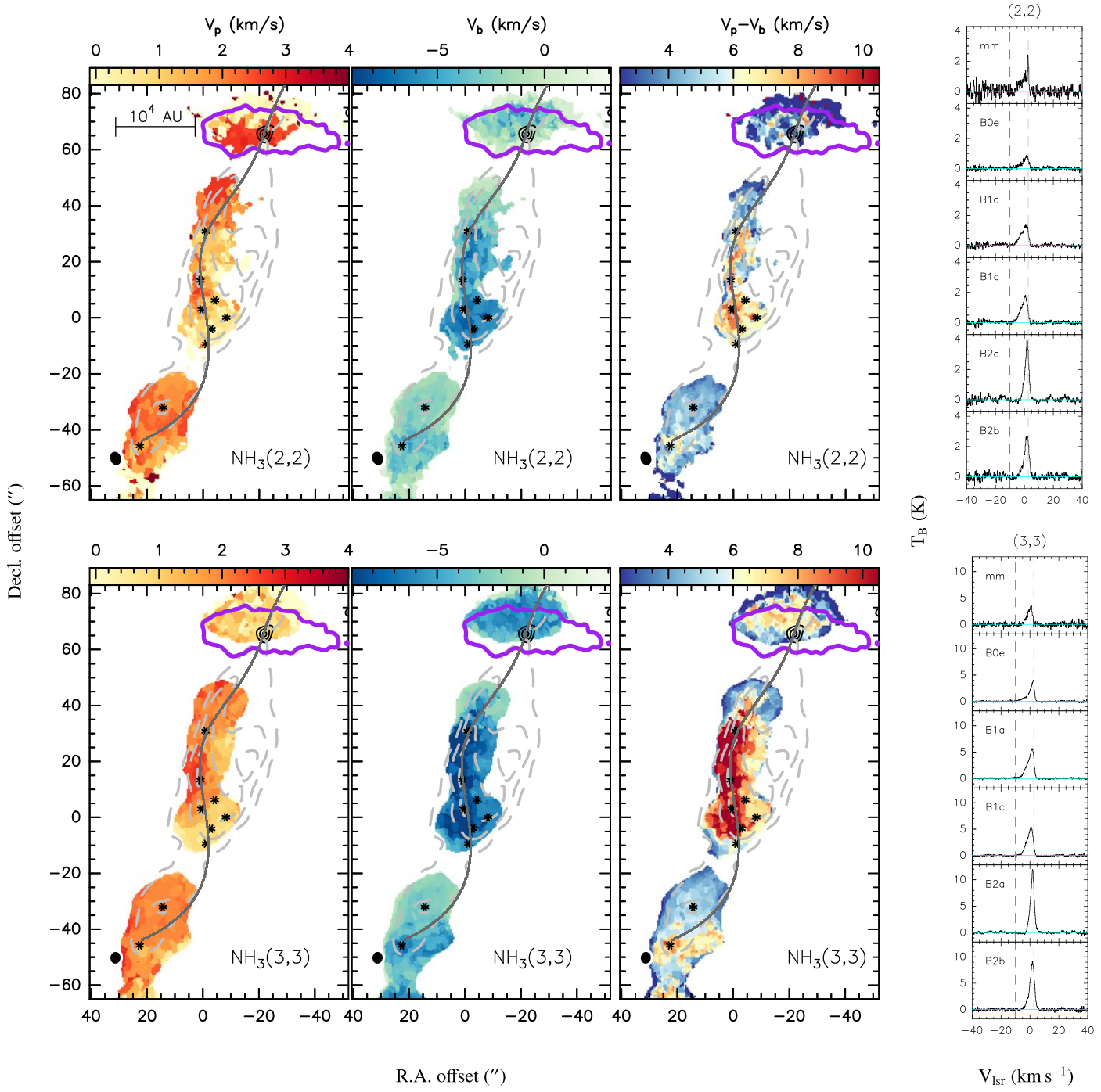

Figure 2. The velocity structure from the cavity wall B0 to shocks B1 and B2 (the same for both cases with or without pb correction). The three left columns show the velocity structure maps of the (2,2) and (3,3) lines. The background in each panel shows the velocity map V_p, where the line intensity peaks (the first column), V_b, where the blueshifted wing extends to (the second column), and the peak-to-bluest velocity offset $V_p - V_b$ (the third column). All maps are naturally weighted. The black contours are the same continuum emissions as those in Figure 1. The purple contour indicates the 5σ emission from the (1,1) integrated intensity toward the flattened envelope around the protobinary system, which is perpendicular to the outflow direction. The gray dashed contours and the labeled clumpy substructures are the same as shown in Figure 1, and the synthesized beam is plotted in the bottom-left corner. The pb-corrected line emissions with $< 5\sigma$ rms are blank in each panel. The black curve guides the path of the precessing jet from L1157-mm as modeled by Podio et al. (2016). The last column shows the (2,2) and (3,3) line profiles extracted from clumpy substructures along the jet path. The gray dashed vertical line indicates the system velocity of the cloud $V_{sys} = 2.7$ km s^{-1}, and the red dashed vertical line indicates the velocity where the main component of each line blueward $V_{lsr} = -10$ km s^{-1}. The line intensity Jy beam^{-1} is converted to the brightness temperature T_B, and the horizontal cyan line indicates the baseline ($T_B = 0$ K). A narrow feature appears toward the protobinary system mm on the spectrum, probably tracing the quiescent and cold gas in the flattened envelope.

deceleration effect of the underlying jet or wind after traveling large distances (Zhang et al. 2000). In each shock, the pattern of blueshifted wings becoming broader with the distance from the outflow source indicates the "Hubble-law", which is modelled as a consequence of the bow shock (e.g., Smith et al. 1997; Downes & Ray 1999).

When comparing the peak-to-bluest velocity offset ($V_p - V_b$) in the line of sight, we note that a high offset of 10 km s^{-1} is present along the curved jet path.

4. Analysis and Discussion

To determine the temperature and density profile over a region in the ISM, the rotational diagram (RD) method was previously widely used with two assumptions: (1) All lines are in the local thermal equilibrium (LTE) condition; (2) the lines are optically thin or the optical depth is known to allow correction. However, our test of the RD method shows that significant blueshifted emissions on the line profiles toward this shocked region lead to large parameter uncertainties (see Appendix C for details).

Instead, with a proper assumption of the source geometry, the large velocity gradient (LVG) escape probability approximation is preferred to constrain the gas properties toward a particular location, when the collision rates of a particular species are known (Sobolev 1960; Goldreich & Scoville 1976).

4.1. LVG Approximation

Using the non-LTE statistical equilibrium radiative transfer code RADEX (van der Tak et al. 2007) and a related solver (Fujun Du's `myRadex`),[18] we apply the MultiNest Algorithm (Feroz & Hobson 2008; Feroz et al. 2009, 2019) and derive the probability density function (PDF) of the kinetic temperature $T_{\rm kin}$, the H_2 volume density n, and the column density N_T for p-NH_3 and o-NH_3 toward all pixels.

Radiative and nonreactive collisional transitions in the gas phase do not change the molecular spin orientations. Therefore, we treat o/p-NH_3 as distinct species and assume that the transitions between them are forbidden (interconversion processes between o- and p-transitions are ignored). In this work, the collision rates are relative to the sum of all the hyperfine components and between NH_3 (1,1)–(6,6) and p-H_2, which are provided by the Leiden Atomic and Molecular Database (LAMDA, Schöier et al. 2005).[19]

All the pb-corrected images are smoothed to the same angular resolution (i.e., $4\farcs90 \times 3\farcs81$) and the same pixel size (i.e., $0\farcs5$). The intensities of the lines are integrated over the velocity range of -25 to $+25$ km s^{-1} by assuming a single velocity component. The geometry is set as "LVG" ("Slab" was tested and no appreciable differences were shown). The FWHM line widths of all lines are adopted as 4 km s^{-1} based on the median from all spectrum fittings (see Table A2). In the case where multivelocity components are smeared within the VLA's synthesized beam, an FWHM line width of 9 km s^{-1} is adopted from Bachiller et al. (1993) and Lefloch et al. (2012) for the test. Two different values have been considered for the beam-filling factor: (i) unity for all lines; and (ii) 0.5 or 0.1 for transitions higher than (3,3). The best-fit parameters are searched over relatively large ranges for the H_2 number density n (10^3–10^7 cm^{-3}), $T_{\rm kin}$ (5–10^4 K), and N_T (10^{14}–10^{17} cm^{-2}).

An example of the PDF from the LVG approximation is shown toward B1a in Figure D1, and examples of parameter maps are given in Figure D2. With different line-width and beam-filling factor combinations, the best fits toward all nine clumps are listed in Table D1. Although degeneracy among the above three parameters is inevitable, we found that the $T_{\rm kin}$ and the N_T for o- and p-NH_3 are well constrained toward these representative positions, with uncertainties less than 30%.

From Figure D1 we also note that the n of each clump cannot be constrained from the LVG fittings, and thus, varying its value in the aforementioned range does not change the best-fit result of $T_{\rm kin}$ and the N_T. In this warm shocked environment, the critical densities of all seven NH_3 lines are in the range of 5×10^3–3×10^4 cm^{-3} (estimated by using the Einstein coefficients and the collision rates provided by LAMDA in the temperature range of 50–300 K, which are consistent with the effective critical density given by, e.g., Shirley 2015). Previous CO and CS observations from Lefloch et al. (2012), Benedettini et al. (2013), and Gómez-Ruiz et al. (2015) indicate $n > 10^4$ cm^{-3} at an angular resolution in the range of 3″–20″, which should validate the LTE assumption for the NH_3 lines. Because this number density cannot be confirmed from our LVG fittings, the RD method would need to be applied with caution.

Our tests show that a smaller beam-filling factor for higher transitions result in better consistency of the $T_{\rm kin}$ derived from o-/p-NH_3 separately (Table D1). The collisional coefficients, the line width, and the integrated intensity of each line adopted in the fittings change the best-fit absolute value of $T_{\rm kin}$ and N_T toward individual pixels, though they do not change the contrast between pixels for both parameter maps (see Appendix D for details).

4.2. The Gas Kinetic Temperature Map

Assuming a line width of 4 km s^{-1}, a unity beam-filling factor for (1,1)–(3,3), and 0.1 for (4,4)–(7,7), Figure 3 shows the maps of gas kinetic temperature, the relative abundance ratio between o- and p-NH_3 and their total column density derived from the above-mentioned LVG best fit.

In a 0.1 pc scale field of view, good agreement on $T_{\rm kin}$ derived from o/p-NH_3 separately (relative ratio ∼1, shown in yellow in the first column of Figure 3, with <10% uncertainty) indicates the appropriateness of these assumptions.

Throughout the entire southern outflow shocks, the mean $T_{\rm kin}$ map reveals an intrinsic gradient (second column of Figure 3): warm components (>120 K) appear toward the spots where the jet impinges on the eastern cavity walls (B0a–B0e–B1a), cool components (<80 K) toward the cavity B1b–B1c and the older shock B2.

Although the temperature gradient from B0 to B2 has been roughly indicated by previous observations (e.g., Umemoto et al. 1999; Tafalla & Bachiller 1995) and was proposed by the model (e.g., Lefloch et al. 2012; Podio et al. 2014 suggested a slightly larger temperature gradient from B0 with > 200 K to B1 with ∼60 K and B2 with ∼20 K), it has never been confirmed by a detailed map until this work. At a linear resolution of ∼1500 au, our refined results indicate that the older components have experienced more postshock cooling.

4.3. The Column Density Map and the Ortho-to-para Ratio Map of NH_3

Given that no continuum at millimeter and centimeter wavelengths is detected toward B0–B1–B2 from the existing data and that the molecular abundance with respect to H_2

[18] https://github.com/fjdu/myRadex

[19] No data are provided for the collision rate between NH_3 (7,7) and p-H_2 in LAMDA.

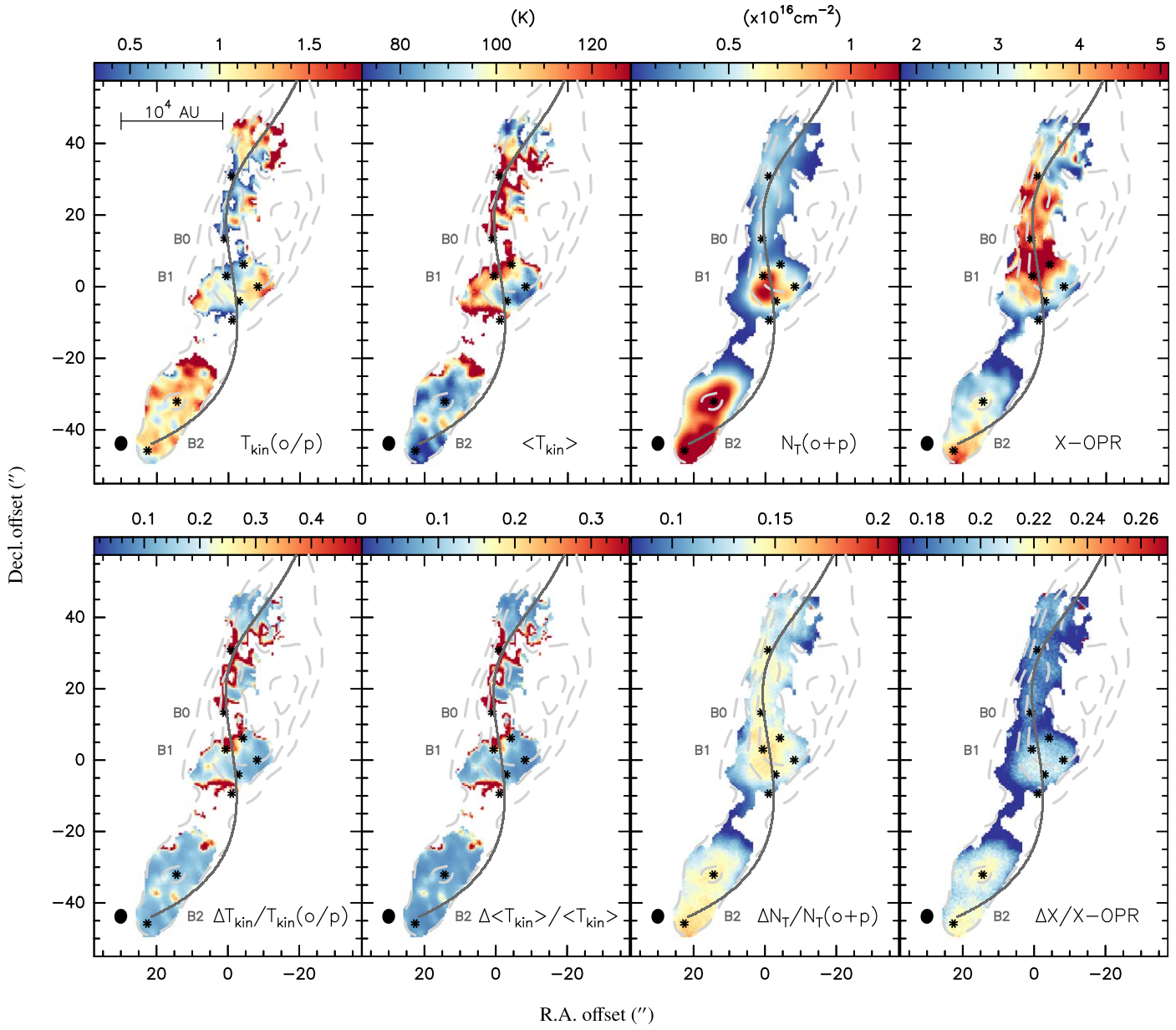

Figure 3. Kinetic temperature maps and column density maps for *o*- and *p*-NH_3, derived from LVG MultiNest best fitting, by assuming a single component (with an FWHM line width of 4 km s^{-1}) and two filling factors (1 for (1,1)–(3,3) lines and 0.1 for (4,4)–(7,7) lines) toward each position. Panels from left to right in the upper row show the relative ratio and the mean of T_{kin} from *o*-/*p*-NH_3, as well as the total column density and the OPR of NH_3. Panels in the lower row show the uncertainty with respect to the value of the above parameters. The pixels where the pb-corrected NH_3 (5,5) and (6,6) lines $< 5\sigma$ emission and CO(1–0) $< 8\sigma$ emission are blank. The gray dashed contours and the labeled clumpy substructures are the same as shown in Figure 1. The black curve guides the path of the precessing jet from L1157-mm as modeled by Podio et al. (2016). These maps are derived by smoothing all lines to the same pixel size and angular resolution, i.e., $4\farcs90 \times 3\farcs81$, shown as the synthesized beam in the bottom left of each panel.

measured from different observations has a large uncertainty especially in the shocked region, the column density and ortho-to-para ratio (OPR) of NH_3 are more reliable physical indicators than its abundance with respect to H_2 in this work.

A U-shape structure appears on both the *o*- and *p*-NH_3 column density map toward B1, connecting the spots B1a–B1c–B1b, with the total value reaching $>1 \times 10^{16}$ cm^{-2} to the eastern wall. Two U-shape structures also appear toward B2a and B2b, with the column density peak twisting toward the western wall (third column of Figure 3). These U-shapes are significant on the integrated intensity maps, especially for the lines observed with a larger pb.

Measuring the Spearman's rank correlation[20] coefficient ρ (Cohen 1988), the total column density shows moderate (0.4–0.5) spatial correlation with the velocity offset in the line of sight ($V_p - V_b$) toward B0 and B2 locally, as well as strong (0.63) correlation toward B1 locally (Figure D3). However, the correlation is weak (0.18) if treating the successively shocks as one entity. This could imply that the sputtering of ammonia off

[20] The Spearman rank correlation coefficient ρ is a nonparametric measure of statistical dependence between two variables. This coefficient can assess how well a monotonic function (no matter whether it is linear or not) can describe the relationship between two variables. The coefficient ρ is in the range from –1 (decreasing monotonic relation) to 1 (increasing monotonic relation), with zero indicating no correlation.

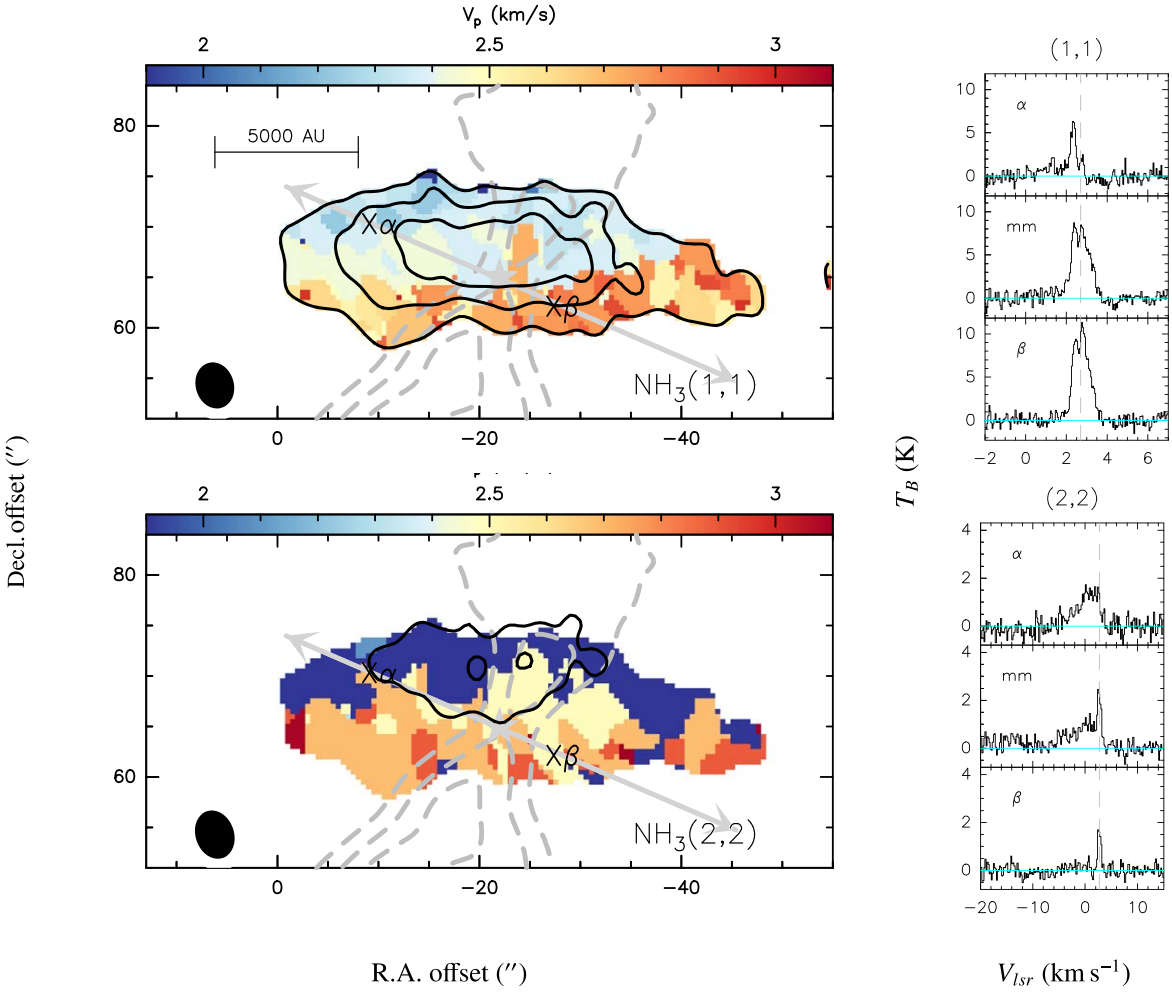

Figure 4. Left column: the V_p map of the main hyperfine component of the (1,1) and (2,2) lines toward the flattened envelope around the marked protobinary system, which should elongate in the direction shown as the gray two-headed arrow (Chiang et al. 2010), perpendicular to the outflow. In each panel, the black contours indicate the integrated intensity (with pb correction), starting from 5σ and increasing by 3σ. The gray dashed contours, starting from 4σ ($\sigma = 0.27$ Jy beam^{-1}) and increasing with the step of 5σ, show the CO (1-0) emission (Gueth et al. 1996), and the synthesized beam is plotted in the bottom-left corner. The pb-corrected (1,1) line emissions with $<5\sigma$ rms are blank in each panel. Right column: beam-averaged line profiles extracted from the protobinary system and two positions perpendicular to the outflow direction in the flattened structure (labeled as α and β on the V_p map). The gray dashed vertical line indicates the $V_{sys} = 2.7$ km s^{-1} of the cloud. The line intensity Jy beam^{-1} is converted to the brightness temperature T_B, and the horizontal cyan line indicates the baseline (T_B= 0 K).

the surface of ice grains is not very sensitive to shock at a velocity up to $\sim$10 km s^{-1}, possibly indicating that NH_3 is efficiently returning in the gas phase already at the lowest values of $V_p - V_b$ (which may then be related to the shock velocity threshold for ice sputtering).

The OPR seems more enhanced along the curved jet path (B0a–B0e–B1a–B1c–B2b) compared to the rest by a factor of 2–2.5 (the fourth column of Figure 3). Interestingly, these locations where the OPR reaches a maximum (as high as 4–5 or 2.8–3.5 when adopting a line width of 4 km s^{-1} or 9 km s^{-1}, respectively) are spatially coincident with the largest velocity offset in the line of sight ($V_p - V_b \sim 10$ km s^{-1}) in Figure 2, showing a strong Spearman's rank correlation ($\rho > 0.5$) toward the entire mapping region (Figure D3). Although the locations of the maximum OPR and the total column density peak are not identical, the Spearman's rank correlation between these parameters is strong ($\rho > 0.5$) toward B0, B1, and B2 locally. Such spatial correlation has also been reported toward other protostellar shocked regions (e.g., shocks associated with Orion-KL, Goddi et al. 2011).

Considering that the uncertainties from observation, data reduction, and LVG estimations (<15%) are uniform for the entire map, we believe the enhancement of column density toward the cavity, the enhancement of OPR toward the jet path, as well as its spatial correlation with the velocity offset are intrinsic dynamic effects.

The OPR gradient revealed by our observations at high angular resolution improves the single-dish result from Umemoto et al. (1999).[21] Enlightened by the explanation from the comprehensive gas-grain chemical network in Harju et al. (2017), surface and gas-phase processes may have different contributions along the cavity walls and within the cavity. According to Faure et al. (2013), OPR < 1 can be reproduced if H_2 is mainly in para form. Therefore, a high OPR (2–5) given from our study may be the result of o-H_2, which is not included in our LVG fitting but whose abundance may indeed increase as expected in shocked gas (see discussion in Appendix D).

[21] Umemoto et al. (1999) assumed all lines are optically thin and reported the OPR toward B1 to be $\sim 1.7^{+0.2}_{0.3}$, while toward B2 to be $\sim 1.7 \pm 0.2$.

4.4. The Flattened Envelope

Previous studies have revealed that the flattened structure surrounding L1157-mm is a mixture of outflow components with the inner envelope on the scale of thousands of astronomical units (e.g., Looney et al. 2007; Chiang et al. 2010; Tobin et al. 2010; Lee et al. 2012). Although the protobinary system mm is at the edge of our pb where the noise level is high from the pb-corrected images (Figures A1–B1), line emissions especially those from (1,1) and (2,2) have $S/N > 3$.

To study the velocity gradient across the flattened envelope, we present the V_p maps of both lines within the region where the (1,1) line shows $>5\sigma$ emission after pb correction (Figure 4). Comparing the beam-averaged line profiles from the protobinary system mm, a northeast position α, and a southwest position β perpendicular to the outflow, we find that a 1 km s^{-1} width narrow feature appears toward the mm on the spectra of the (2,2) line. Such feature appears on the (3,3) line as well (Figure 2), probably tracing the quiescent and cold gas in the flattened envelope. The blueshifted wing may trace the warmer material partially belonging to the outflow.

A velocity gradient of the N_2H^+ (1–0) line is reported by Chiang et al. (2010) and Tobin et al. (2010), which is normal to the outflow elongation and indicates the presence of rotation. In contrast, our NH_3 lines present a velocity gradient from the northeast ($\sim$2 km s^{-1}) to the southwest ($\sim$3 km s^{-1}). Nevertheless, this gradient is the same as what was shown on the JVLA NH_3 (1,1) map by Tobin et al. (2010), covering $\pm 30''$ east and west offset to the protobinary system mm. Another consistency with Tobin et al. (2010) is the redshifted ($\sim$2.7 km s^{-1}) gas of NH_3, which seems to be curved down toward B0. Therefore, instead of an effect of sidelobe contamination (e.g., in dark blue on the (2,2) map of Figure 4), we believe the northeast to southwest velocity gradient of the NH_3 lines indicates the interaction between the outflow and the envelope.

5. Conclusions

Our newest JVLA observations provide high-sensitivity images of NH_3 (1,1)–(7,7) lines toward the archetypal protostellar shock, which is associated with the chemically rich blueshifted outflow in L1157. In the 0.1 pc scale field of view, we draw detailed kinetic temperature and NH_3 column density maps of this successively shocked region for the first time at a linear resolution of 1500 au. Our conclusions are as follows:

1. The emissions of all seven lines highlight the curved precessing jet path, from the eastern cavity wall of B0 and B1 to the cavity B2. In the line of sight, the map of the peak-to-bluest velocity offset reaches as high as 10 km s^{-1} on this path.
2. Treating *o*- and *p*-NH_3 as distinct species, the kinetic temperature maps from LVG fittings show good agreement. The high-precision ($<$10% uncertainty) temperature map reveals an intrinsic gradient from the warm B0 eastern cavity wall ($>$120 K) to the cool cavity B1 and the earlier shock B2 ($<$80 K).
3. Both *o*- and *p*-NH_3 show a column density enhancement toward three U-shape cavities in B1 and B2, reaching as high as $>1\times10^{16}$ cm^{-2}. The OPR is enhanced by a factor of 2–2.5 along the curved jet path compared to the rest, showing a strong spatial correlation with the peak-to-bluest velocity offset and with the total column density. All of these chemical gradients may be linked to the shocks.
4. A flattened envelope surrounding the protobinary system appears at the edge of our pb. We find a 1 km s^{-1} width narrow feature on the line spectrum, probably tracing the quiescent and cold gas in the flattened envelope. The velocity map for the line intensity peak velocity shows a gradient from the northeast ($\sim$2 km s^{-1}) to the southwest ($\sim$3 km s^{-1}) of this structure, with the redshifted ($\sim$2.7 km s^{-1}) gas extended toward B0, indicating the interaction between the outflow and the envelope.

We gratefully acknowledge the useful and complimentary comments of the anonymous referee.

H.B.L. is supported by the Ministry of Science and Technology (MoST) of Taiwan (grant Nos. 108-2112-M-001-002-MY3).

F.D. is supported by the National Natural Science Foundation of China (NSFC) through grant Nos. 11873094 and 12041305.

C.Co. acknowledges the PRIN-INAF 2016 "The Cradle of Life—GENESIS-SKA (General Conditions in Early Planetary Systems for the rise of life with SKA)."

C.C. acknowledges receiving funds from the European Union's Horizon 2020 research and innovation programme from the European Research Council (ERC) for the project "The Dawn of Organic Chemistry" (DOC), grant agreement No. 741002, and from the Marie Sklodowska-Curie for the project "Astro-Chemical Origins" (ACO), grant agreement No. 811312.

This research made use of NASA's Astrophysics Data System.

Software: astropy (Astropy Collaboration et al. 2013), Numpy (van der Walt et al. 2011), CASA (v5.4.0; v5.6.1; McMullin et al. 2007), `bettermoments` (v1.0.0; Teague & Foreman-Mackey 2018), `HfS` (Estalella 2017).

Appendix A
Line Profile

Along the jet paths, the protobinary system L1157-mm and nine representative clumpy substructures from B0 to B1 and B2 are denoted, with their coordinates listed in Table A1. The beam-averaged line profiles of NH_3 (1,1)–(7,7) are extracted from these nine positions, shown in Figure A1.

Table A1
Positions Corresponding to the Protostellar Object and the Clumpy Substructures

	R.A. (J2000)	Decl. (J2000)
mm	$20^h39^m06\overset{s}{.}170$	68°02′15.07s″
B0a	$20^h39^m10\overset{s}{.}026$	68°01′41.30s″
B0e	$20^h39^m10\overset{s}{.}365$	68°01′23.80s″
B1a	$20^h39^m10\overset{s}{.}301$	68°01′13.51s″
B1b	$20^h39^m08\overset{s}{.}734$	68°01′10.54s″
B1c	$20^h39^m09\overset{s}{.}677$	68°01′06.45s″
B1f	$20^h39^m09\overset{s}{.}444$	68°01′16.70s″
B1i	$20^h39^m10\overset{s}{.}000$	68°01′01.11s″
B2a	$20^h39^m12\overset{s}{.}755$	68°00′38.44s″
B2b	$20^h39^m14\overset{s}{.}217$	68°00′24.73s″

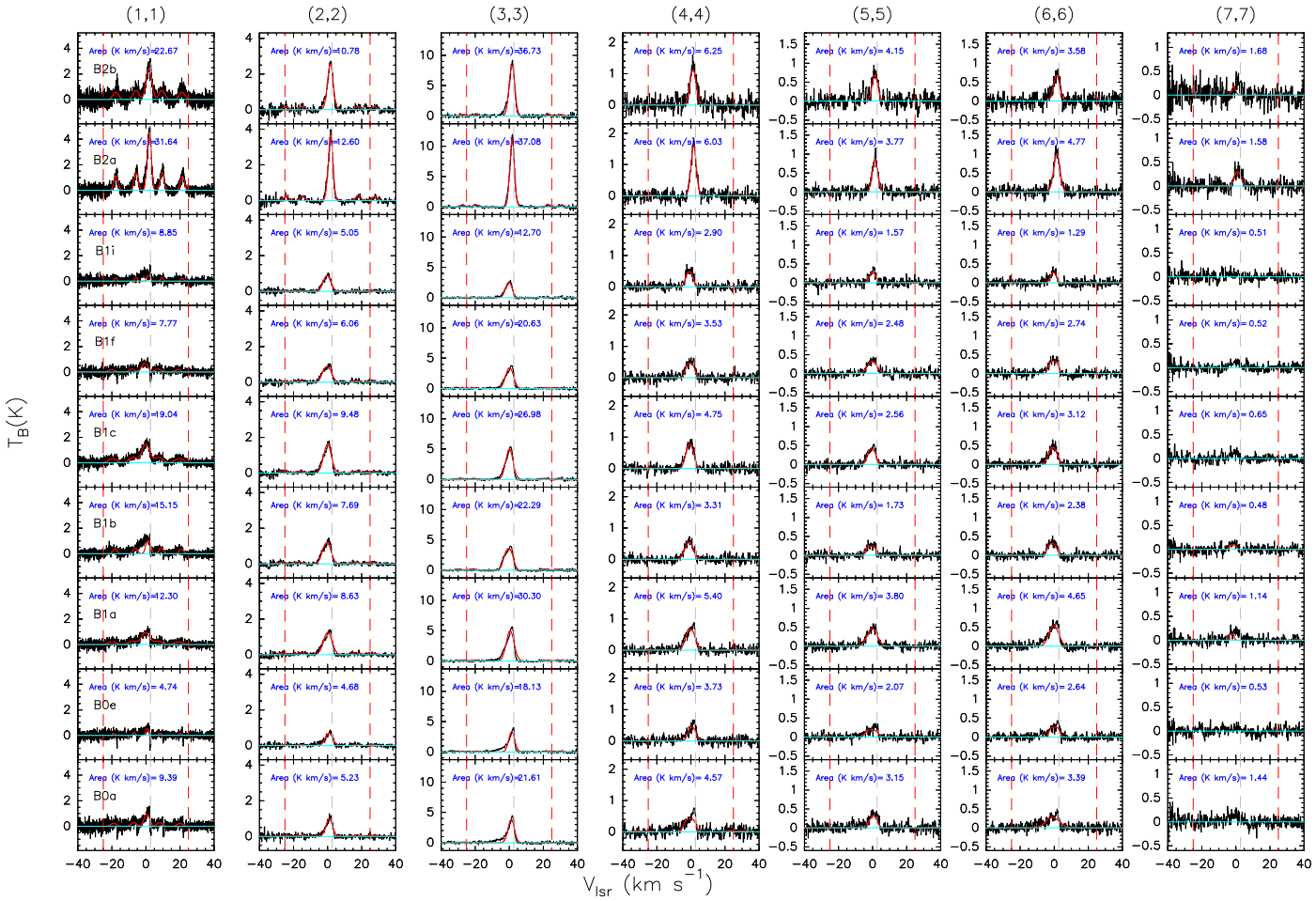

Figure A1. Beam-averaged line profiles (the line intensity Jy beam^{-1} is converted to the brightness temperature T_B), with the center toward nine clumpy substructures (Table A1) in the plane of the sky. The `HfS` fit is shown in red overlying each spectrum. All lines are extracted from images smoothed to the same pixel size ($0\farcs5$), and their velocity resolutions are listed in Table 1. In each panel, two red vertical lines at –25 and + 25 km s^{-1} indicate the velocity range within which we integrate the intensity; the gray dashed vertical line indicates the $V_{sys} = 2.7$ km s^{-1} of the cloud. The horizontal cyan line indicates the baseline ($T_B = 0$ K).

Applying the Monte Carlo fitting tool `HfS` developed by Estalella (2017), we fit the hyperfine multiplets of each line with a Gaussian shape model using the "hfs_fit" procedure and assuming one velocity component. The best-fit results of the line parameters are listed in Table A2 and shown as a red curve overlying the observation spectrum in Figure A1.

Testing the other mainstream fitting packages, such as CLASS/GILDAS (Pety 2005) and `PySpecKit` (Ginsburg & Mirocha 2011), we found similar fitting results.

Given that the following assumptions were made in these mainstream fitting packages, some caveats need to be noted:

(1) The mainstream fitting packages take the Gaussian profile as a model, but our target lines show significant blueshifted emissions in this successive shocked region. Therefore, the centroid velocity of the main component is not strictly identical to the velocity of the peak intensity, and the FWHM line width from fitting is slightly narrower than the observed line wing, especially for the (3,3)–(6,6) lines (Figure A1).

(2) The mainstream fitting packages provide the optical depth of the main component τ_m. This optical depth is close to that of the entire line τ, but only when the satellites have <30% contribution to the line-integrated intensity, i.e., for the (2,2)–(7,7) lines. As to the (1,1) line where satellites may also be optically thick, τ_m may be significantly smaller than τ.

(3) As a compromise of the fit to hyperfine multiplets, one velocity component is assumed in the fitting. This may bring in an overestimation of the FWHM line width.

Table A2
The Best-fit Parameters for Spectra in Figure A1

Position	Best-fit parameter[a]	(1,1)	(2,2)	(3,3)	(4,4)	(5,5)	(6,6)	(7,7)
B0a	δV(km s^{-1})[b]	3.59 ± 0.56	4.47 ± 0.50	4.34 ± 0.21	4.64 ± 1.75	4.80 ± 0.65	9.60 ± 2.79	...[h]
	$V_{\rm lsr}$(km s^{-1})[c]	0.56 ± 0.20	1.02 ± 0.19	1.19 ± 0.08	-0.61 ± 0.89	0.38 ± 0.44	-0.93 ± 1.18	...[h]
	A$(1-e^{-\tau_m})$(K)[d,e]	1.04 ± 0.11	1.07 ± 0.10	3.60 ± 0.13	0.46 ± 0.11	0.37 ± 0.05	0.31 ± 0.07	...[h]
	$\tau_m^* = 1 - e^{-\tau_m}$	0.26 ± 0.43	(4.0 ± 4.0)E $-$ 4	(2.0 ± 2.0)E $-$ 4	1.00 ± 0.07[g]	0.72 ± 0.46[g]	(4.0 ± 4.0)E $-$ 4	...[h]
	I(K km s^{-1})[f]	$9.54^{+0.36}_{-3.64}$	$7.00^{+0.33}_{-1.40}$	$23.44^{+0.49}_{-2.02}$	$5.28^{+0.27}_{-1.09}$	$2.94^{+0.07}_{-0.26}$	$3.66^{+0.12}_{-0.78}$	$1.17^{+0.17}_{-0.08}$
B0e	δV(km s^{-1})[b]	1.57 ± 0.53	4.94 ± 1.67	4.11 ± 0.25	4.31 ± 0.45	5.29 ± 4.98	3.82 ± 0.63	...[h]
	$V_{\rm lsr}$(km s^{-1})[c]	0.77 ± 0.01	0.88 ± 0.24	1.49 ± 0.09	0.66 ± 0.33	-0.53 ± 0.98	0.20 ± 0.34	...[h]
	A$(1-e^{-\tau_m})$(K)[d,e]	0.63 ± 0.14	0.75 ± 0.08	3.15 ± 0.14	0.49 ± 0.05	0.22 ± 0.07	0.29 ± 0.03	...[h]
	$\tau_m^* = 1 - e^{-\tau_m}$	0.80 ± 0.16	0.45 ± 1.49[g]	(5.0 ± 5.0)E $-$ 4	0.90 ± 0.14[g]	0.99 ± 0.44[g]	1.00 ± 0.02[g]	...[h]
	I(K km s^{-1})[f]	$4.94^{+0.43}_{-1.52}$	$6.46^{+0.42}_{-1.65}$	$19.88^{+0.44}_{-1.66}$	$3.86^{+0.16}_{-0.42}$	$2.23^{+0.13}_{-0.19}$	$2.37^{+0.07}_{-0.09}$	$0.57^{+0.16}_{-0.07}$
B1a	δV(km s^{-1})[b]	5.46 ± 0.39	5.57 ± 0.49	5.34 ± 0.17	5.36 ± 0.33	6.87 ± 0.65	6.40 ± 0.39	1.78 ± 4.53
	$V_{\rm lsr}$(km s^{-1})[c]	-0.22 ± 0.18	0.13 ± 0.14	0.58 ± 0.07	-0.21 ± 0.22	-0.17 ± 0.27	-0.21 ± 0.23	-2.37 ± 0.08
	A$(1-e^{-\tau_m})$(K)[d,e]	1.00 ± 0.07	1.28 ± 0.06	4.67 ± 0.12	0.71 ± 0.04	0.50 ± 0.04	0.57 ± 0.03	0.18 ± 0.04
	$\tau_m^* = 1 - e^{-\tau_m}$	0.27 ± 0.28	0.50 ± 0.33	(3.1 ± 3.1)E $-$ 3	0.83 ± 0.10	0.01 ± 0.01	0.53 ± 0.22	1.00 ± 0.01
	I(K km s^{-1})[f]	$12.46^{+0.14}_{-4.57}$	$10.68^{+0.42}_{-2.16}$	$32.76^{+1.04}_{-2.35}$	$5.35^{+0.11}_{-0.17}$	$4.01^{+0.06}_{-0.35}$	$4.58^{+0.08}_{-0.12}$	$1.53^{+0.02}_{-0.18}$
B1b	δV(km s^{-1})[b]	2.72 ± 4.35	5.30 ± 0.44	4.83 ± 0.28	5.72 ± 0.64	3.62 ± 0.73	4.46 ± 0.39	3.56 ± 1.26
	$V_{\rm lsr}$(km s^{-1})[c]	1.41 ± 0.01	-0.41 ± 0.13	-0.37 ± 0.07	-1.07 ± 0.28	-0.97 ± 0.50	-1.24 ± 0.30	-1.68 ± 0.62
	A$(1-e^{-\tau_m})$(K)[d,e]	1.11 ± 0.14	1.24 ± 0.06	3.50 ± 0.08	0.60 ± 0.06	0.28 ± 0.04	0.35 ± 0.03	0.14 ± 0.04
	$\tau_m^* = 1 - e^{-\tau_m}$	0.84 ± 0.13	0.55 ± 0.28	0.76 ± 0.13	(1.8 ± 1.8)E $-$ 3	1.00 ± 0.03[g]	0.95 ± 0.08[g]	0.95 ± 0.72[g]
	I(K km s^{-1})[f]	$15.15^{+0.04}_{-5.97}$	$9.00^{+0.41}_{-1.24}$	$23.90^{+0.49}_{-0.93}$	$3.42^{+0.20}_{-0.25}$	$2.59^{+0.22}_{-0.57}$	$2.59^{+0.05}_{-0.21}$	$0.84^{+0.15}_{-0.11}$
B1c	δV(km s^{-1})[b]	5.30 ± 0.25	5.37 ± 0.22	4.97 ± 0.13	4.64 ± 0.28	4.15 ± 0.31	5.75 ± 0.71	...[h]
	$V_{\rm lsr}$(km s^{-1})[c]	0.00 ± 0.12	0.00 ± 0.09	0.11 ± 0.05	-0.60 ± 0.19	-0.53 ± 0.24	-0.79 ± 0.29	...[h]
	A$(1-e^{-\tau_m})$(K)[d,e]	1.51 ± 0.07	1.65 ± 0.06	4.67 ± 0.10	0.82 ± 0.05	0.44 ± 0.03	0.50 ± 0.05	...[h]
	$\tau_m^* = 1 - e^{-\tau_m}$	0.32 ± 0.17	0.03 ± 0.03	0.02 ± 0.02	0.76 ± 0.13	0.96 ± 0.05[g]	(1.0 ± 1.0)E $-$ 4	...[h]
	I(K km s^{-1})[f]	$19.08^{+0.09}_{-7.36}$	$11.20^{+0.70}_{-1.55}$	$29.59^{+0.59}_{-1.61}$	$5.38^{+0.03}_{-0.37}$	$3.22^{+0.14}_{-0.44}$	$3.20^{+0.01}_{-0.04}$	$1.10^{+0.09}_{-0.18}$
B1f	δV(km s^{-1})[b]	3.88 ± 0.36	5.32 ± 0.53	5.00 ± 0.52	4.02 ± 0.33	6.37 ± 0.84	4.15 ± 0.32	...[h]
	$V_{\rm lsr}$(km s^{-1})[c]	-0.66 ± 0.01	-0.27 ± 0.16	0.24 ± 0.09	-0.37 ± 0.27	-0.11 ± 0.35	-0.38 ± 0.28	...[h]
	A$(1-e^{-\tau_m})$(K)[d,e]	0.76 ± 0.08	0.92 ± 0.05	3.26 ± 0.09	0.50 ± 0.04	0.37 ± 0.04	0.37 ± 0.03	...[h]
	$\tau_m^* = 1 - e^{-\tau_m}$	0.58 ± 0.28	0.65 ± 0.27[g]	0.44 ± 0.43	0.97 ± 0.04[g]	0.09 ± 0.09	0.99 ± 0.02[g]	...[h]
	I(K km s^{-1})[f]	$7.44^{+0.03}_{-2.69}$	$7.44^{+0.25}_{-1.36}$	$22.54^{+0.35}_{-1.74}$	$3.22^{+0.35}_{-0.14}$	$2.59^{+0.08}_{-0.12}$	$2.95^{+0.03}_{-0.18}$	$0.51^{+0.03}_{-0.19}$
B1i	δV(km s^{-1})[b]	1.52 ± 5.84	5.18 ± 0.34	4.18 ± 0.38	3.64 ± 0.34	4.26 ± 0.80	3.96 ± 0.82	...[h]
	$V_{\rm lsr}$(km s^{-1})[c]	1.86 ± 0.01	-0.26 ± 0.15	-0.21 ± 0.07	-0.84 ± 0.26	0.11 ± 0.34	-0.45 ± 0.34	...[h]
	A$(1-e^{-\tau_m})$(K)[d,e]	0.56 ± 0.07	0.93 ± 0.05	2.44 ± 0.07	0.53 ± 0.05	0.33 ± 0.05	0.32 ± 0.05	...[h]
	$\tau_m^* = 1 - e^{-\tau_m}$	0.99 ± 0.02[g]	(4.0 ± 4.0)E $-$ 4	0.39 ± 0.39	0.95 ± 0.07[g]	(3.0 ± 3.0)E $-$ 4	(5.4 ± 5.4)E $-$ 3	...[h]
	I(K km s^{-1})[f]	$9.61^{+0.04}_{-3.68}$	$5.73^{+0.24}_{-0.68}$	$13.96^{+0.37}_{-0.93}$	$3.73^{+0.35}_{-0.71}$	$1.56^{+0.11}_{-0.14}$	$1.38^{+0.05}_{-0.01}$	$0.61^{+0.07}_{-0.04}$
B2a	δV(km s^{-1})[b]	2.70 ± 0.10	3.21 ± 0.11	3.15 ± 0.05	3.68 ± 0.26	3.82 ± 0.37	4.38 ± 0.33	3.43 ± 3.09
	$V_{\rm lsr}$(km s^{-1})[c]	1.99 ± 0.03	1.81 ± 0.04	1.75 ± 0.02	1.63 ± 0.10	1.47 ± 0.15	1.52 ± 0.12	1.09 ± 0.15
	A$(1-e^{-\tau_m})$(K)[d,e]	4.62 ± 0.13	3.76 ± 0.11	10.29 ± 0.15	1.67 ± 0.10	0.90 ± 0.07	1.05 ± 0.06	0.34 ± 0.12
	$\tau_m^* = 1 - e^{-\tau_m}$	0.31 ± 0.11	(1.0 ± 1.0)E $-$ 3	(2.8 ± 2.8)E $-$ 3	(1.2 ± 1.2)E $-$ 3	(7.0 ± 7.0)E $-$ 4	(2.0 ± 2.0)E $-$ 4	0.97 ± 0.86[g]
	I(K km s^{-1})[f]	$30.82^{+0.18}_{-11.73}$	$15.80^{+1.12}_{-2.93}$	$41.63^{+1.37}_{-3.51}$	$7.14^{+0.06}_{-0.94}$	$3.64^{+0.16}_{-0.03}$	$5.54^{+0.02}_{-0.58}$	$1.62^{+0.04}_{-0.02}$

Table A2
(Continued)

Position	Best-fit parameter[a]	(1,1)	(2,2)	(3,3)	(4,4)	(5,5)	(6,6)	(7,7)
B2b	δV(km s^{-1})[b]	3.86 ± 0.25	3.90 ± 0.22	3.81 ± 0.10	4.24 ± 0.54	3.95 ± 0.68	4.31 ± 0.69	2.74 ± 1.20
	$V_{\rm lsr}$(km s^{-1})[c]	1.81 ± 0.16	1.65 ± 0.08	1.60 ± 0.04	1.33 ± 0.21	1.48 ± 0.26	1.41 ± 0.28	1.44 ± 0.54
	A$(1 - {\rm e}^{-\tau_m})$(K)[d,e]	2.57 ± 0.16	2.68 ± 0.12	7.88 ± 0.18	1.23 ± 0.13	0.78 ± 0.11	0.76 ± 0.10	0.25 ± 0.08
	$\tau_m^* = 1 - e^{-\tau_m}$	0.11 ± 0.12	$(1.3 \pm 1.3){\rm E} - 3$	$(3.0 \pm 3.0){\rm E} - 4$	$(1.0 \pm 1.0){\rm E} - 4$	$(3.3 \pm 3.3){\rm E} - 3$	0.02 ± 0.02	0.97 ± 0.93[g]
	I(K km s^{-1})[f]	$22.30^{+0.10}_{-8.67}$	$14.57^{+0.99}_{-3.07}$	$39.51^{+0.65}_{-2.39}$	$5.88^{+0.59}_{-0.11}$	$4.41^{+0.17}_{-0.58}$	$3.60^{+0.12}_{-0.07}$	$1.88^{+0.1}_{-0.72}$

Notes.
[a] Given by using the "hfs_fit" procedure in the `HfS` package, fit by assuming a Gaussian line profile; all beam-averaged lines are extracted from images with the same pixel size.
[b] Intrinsic FWHM line width by taking into account the opacity.
[c] Centroid velocity of the main component.
[d] Peak intensity of the main component (for lines broader than the channel width).
[e] Optical depth of the main component τ_m, provided by the `HfS` as τ_m^*, $\tau_m = -ln(1 - \tau_m^*)$.
[f] Integrated intensity over the velocity range from –25 to + 25km s^{-1}, the uncertainty is given by the difference between this range and the velocity range of –10 ∼+5 km s^{-1} (the main component of the hyperfine multiplets) and –27 ∼+33 km s^{-1} (line intensity down to zero).
[g] Fitting results need to be taken cautiously for $\tau_m > 1$ and with an uncertainty larger than the value.
[h] Line emission is less than 3σ.

Appendix B
Images with Primary Beam Correction

Given that the beam responses are different for each antenna in a synthesis array, the flux density at the beam edge is biased low. Dividing the image by the pb, we apply the pb correction to each line datacube and provide the integrated intensity maps over the velocity range of -25 to $+25\,\mathrm{km\,s^{-1}}$ in Figure B1. Compared with Figure 1, line emission toward the edge of the pb (e.g., mm, B2b) are recovered. However, noise levels are increasing toward these positions (see example spectrum in Figure 2).

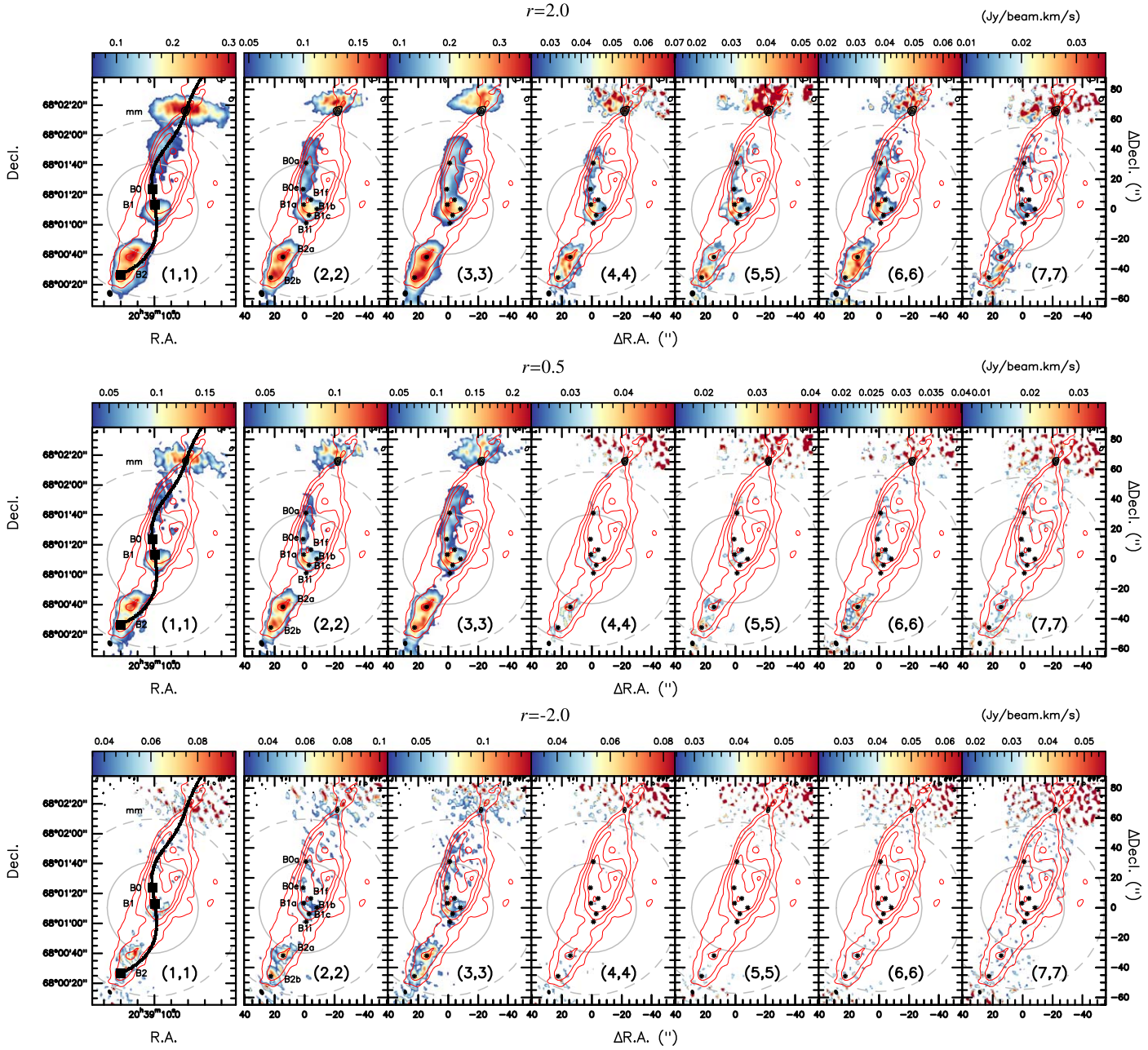

Figure B1. The outline of the southern (blueshifted) outflow lobe from the Class 0 compact protobinary system L1157-mm (images with different weightings are given in different rows). Color maps show the intensity maps of NH_3 (1,1)–(7,7) integrated over the velocity range of -25 to $+25$ km s^{-1} (with pb correction). The black contours, starting from 4σ ($\sigma = 0.03$ mJy beam^{-1}) and increasing with a step of 4σ, show the continuum emission with the same weighting as the line emissions (with pb correction). The rest of the contours and all the labels are the same as in Figure 1. The solid gray circle indicates the largest recoverable scale and the dashed gray circle indicates the primary beam.

Appendix C
Line Optical Depth Correction

Even though the mainstream fitting packages bring in a centroid velocity map a bit different from the peak velocity map (Section A), they can constrain the lower limit of the optical depth for a particular line τ for each pixel. Therein, to correct the molecular column density, which is underestimated, we can multiply the line-integrated intensity from observations by a factor of $\tau/(1-e^{-\tau})$.

Applying the "hfs_cube_mp" procedure in the `HfS` fitting tool, we focus on deriving the optical depth τ_m map and its uncertainty map for each line. Because the parameter directly given by the fitting program is $\tau_m^* = 1 - e^{-\tau_m}$, the error propagation algorithm enhances the uncertainty of τ_m due to the fitting caveats listed in Section A. Therefore, we set a threshold for the pixels with a high fidelity, i.e., when the uncertainty with respect to the value is less than 1 dex.

As shown in Figure C1, the optical depths of all seven lines are negligible ($\tau_m < 1$) toward B2, while those toward the B1 cavity wall (B1a, B1f, B1i, B1b) are larger than 3, except for the (3,3) line. The τ_m of (4,4)–(6,6) may be underestimated toward some pixels, where the uncertainties are higher than the value by a factor of more than 5.

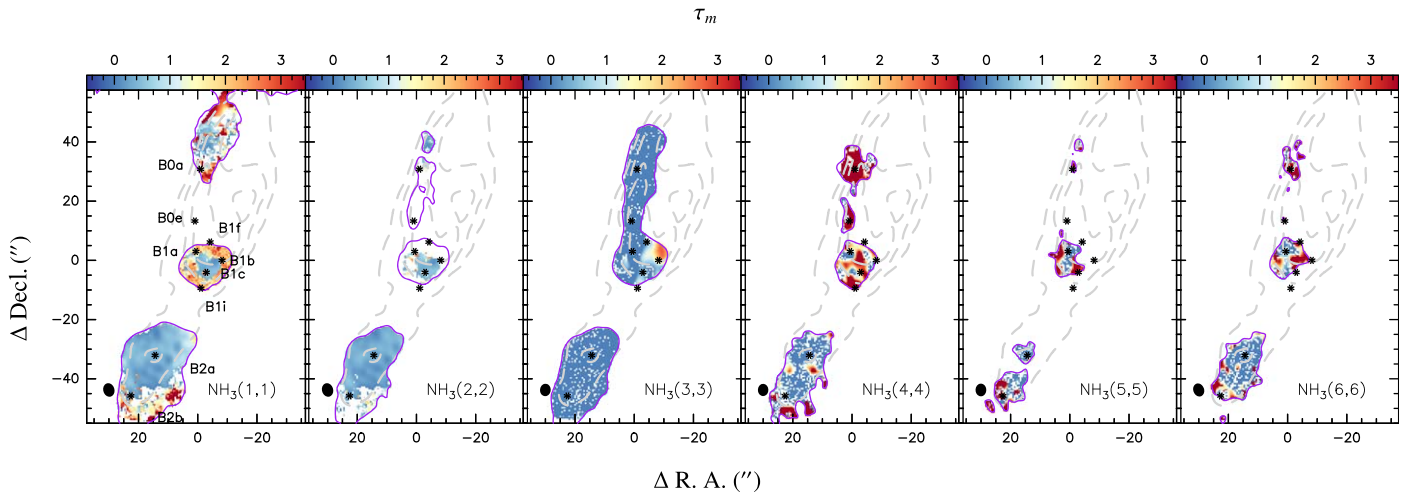

Figure C1. Optical depth τ_m maps of the (1,1)–(6,6) lines. The gray dashed contours and the labeled clumpy substructures are the same as shown in Figure 1. The integrated intensity of the line within the red solid contour shows $>4\sigma$ emissions. The pixels where lines show $<4\sigma$ emissions or uncertainty 1 dex higher than the value of τ_m are blank.

Appendix D
LVG Fitting Example and Caveats

The optical depth of each line is significant, uncertain, and not uniform throughout the entire region. Even correcting each line-integrated intensity with the optical depth τ_m, the rotation diagram (RD) method is not an optimized approach to deriving the temperature and density structure of our source. Instead, the LVG approximation is suitable under such a circumstance, though it is computationally expensive.

Figure D1 gives a PDF example of the $T_{\rm kin}$, N_T, and n from LVG MultiNest fitting toward B1a by treating the o- and p-NH_3 as distinct species. Table D1 lists the mean, standard deviation, and the best fit of $T_{\rm kin}$ and N_T for o/p-NH_3 toward nine clumps. Figure D2 gives a combination of $T_{\rm kin}$ and N_T maps for o/p-NH_3 by testing the cases assuming the beam-filling factor to be unity for all lines and the line width to be $4\,{\rm km\,s^{-1}}$ or $9\,{\rm km\,s^{-1}}$. Figure D3 gives possible spatial correlations between the variables derived from LVG fittings.

One major caveat in the above LVG fitting is that LAMDA only provides the collision rates between the p-/o-NH_3 and p-H_2 (Danby et al. 1988). Although we note that some o-H_2 cross sections were computed at a few selected energies (e.g., Offer & Flower 1989; Rist et al. 1993; Bouhafs et al. 2017), no collision rates between p-/o-NH_3 and o-H_2 are available in LAMDA. Unlike the case in cold dense cores, the abundance of o-H_2 can become significant in warm and shocked regions (e.g., Flower et al. 2006; Neufeld et al. 2019).

A second caveat is the beam-filling factor, which we take as unity for all lines in the fitting, given that the line emissions show more extended spatial distributions toward all the clumpy substructures than the synthesized beam. However, considering that shock discontinuities cannot be spatially resolved by observations, substructures with high column density and high temperature might be beam smeared. This is likely the case after checking the peak brightness temperatures of all transitions toward the representative positions (Figure A1) and their optical depth maps (Figure C1). For testing, we set it as unity for (1,1)–(3,3) and 0.5, or 0.1, or 0.01 for (4,4)–(7,7), and then compare the testing results with the results by assuming the beam-filling factor of unity for all lines. When the filling factor for higher transition levels is adopted in the range of 0.1–1, a smaller filling factor decreases the kinetic temperature significantly, by 30% for p-NH_3 but by <10% for o-NH_3. In contrast, the column density of o/p-NH_3 only shows imperceptible changes (<5%) when a different beam-filling factor is adopted.

A third caveat is the FWMH line width we adopted, i.e., the median from all spectrum fitting as $4\,{\rm km\,s^{-1}}$. This seems to be consistent with the FWHM line width of (1,1)–(3,3) at an angular resolution of 40″, which was reported to be 8–9 $\rm km\,s^{-1}$ by Bachiller et al. (1993). However, the peak-to-bluest velocity offset varies pixel by pixel (Figure 2), being broader along the jet path than within the cavity by a factor of 2. As a compromise to the NH_3 hyperfine multiplets fitting, we assume one velocity component. In the case of multivelocity components being smeared within the VLA's synthesized beam, an FWHM line width of $9\,{\rm km\,s^{-1}}$ is adopted for the test. We find that such a line width leads to a 15% and 20% increase in the best-fit $T_{\rm kin}$ for p-NH_3 and o-NH_3, as well as a 15% and 45% decrease in their N_T, respectively (Table D1). Nevertheless, these increase and decrease factors are globally consistent throughout the entire map pixels, so the contrast (local gradient) of each map does not change.

A minor fourth caveat is the velocity range over which we integrate the line intensity. In Table A2, we list the uncertainty of the line-integrated intensity I, which is given by comparing the integration (i) where the line emission has $S/N > 3$ (–25 to $+25\,{\rm km\,s^{-1}}$); (ii) where the line emission is above zero (–27 to $+33\,{\rm km\,s^{-1}}$), and (iii) includes only the main component of the hyperfine multiplets (–10 to $+5$ $\rm km\,s^{-1}$). Due to strong

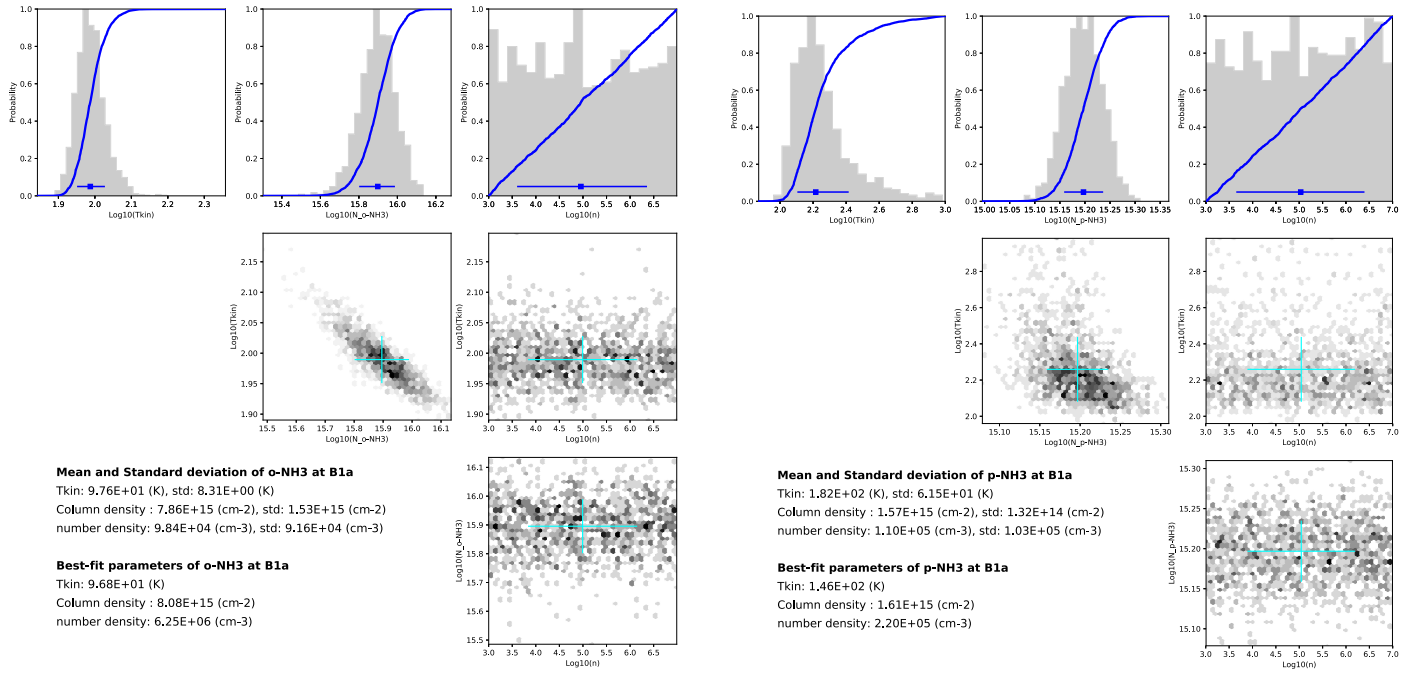

Figure D1. The PDF of o/p-NH_3 parameters toward B1a, derived by using RADEX and the MultiNest algorithm. A line width of 4 $\rm km\,s^{-1}$ is adopted for all lines, and the beam-filling factor is assumed to be unity for the (1,1)–(3,3) lines while to be 0.1 for the (4,4)–(7,7) lines. The fitting parameters, including the H_2 volume density (n), o/p-NH_3 column density N(o/p-NH_3) and the gas kinetic temperature ($T_{\rm kin}$), are listed.

Table D1
Mean and Standard Deviation of the PDF and Best-fit Results Using the LVG Method

Location	Species[a]	ff[b]	$N_{T,n}$[c] (10^{15} cm^{-2})		$T_{\mathrm{kin},n}$[c] (K)		$N_{T,b}$[d] (10^{15} cm^{-2})		$T_{\mathrm{kin},b}$[d] (K)		n[e] (10^5 cm^{-3})
		Case	mean ± std	best fit	mean ± std	best fit	mean ± std	best fit	mean ± std	best fit	best fit
B0a	p-NH_3	I	1.0 ± 0.0	1.1	436 ± 158	327	0.8 ± 0.1	0.9	525 ± 174	802	0.1–8.1
		II	1.0 ± 0.0	1.0	305 ± 124	204	0.9 ± 0.1	0.9	369 ± 145	271	0.03-33.7
	o-NH_3	I	4.2 ± 0.8	4.4	102 ± 8	100	2.6 ± 0.4	2.6	122 ± 11	121	15.2–73.4
		II	4.2 ± 0.8	4.4	102 ± 8	100	2.6 ± 0.4	2.6	122 ± 11	121	0.5–5.0
B0e	p-NH_3	I	0.8 ± 0.0	0.9	278 ± 91	233	0.8 ± 0.1	0.8	386 ± 132	292	4.8–61.4
		II	1.0 ± 0.0	0.9	294 ± 78	196	0.8 ± 0.1	0.8	439 ± 181	198	0.03–0.1
	o-NH_3	I	4.0 ± 0.7	4.2	103 ± 9	102	2.5 ± 0.4	2.6	124 ± 11	122	0.3–4.9
		I	4.1 ± 0.7	4.2	103 ± 9	102	2.5 ± 0.4	2.6	124 ± 11	123	0.8–92
B1f	p-NH_3	I	0.8 ± 0.1	0.8	175 ± 41	154	0.6 ± 0.1	0.7	206 ± 57	178	5.8–46.0
		II	0.8 ± 0.1	0.8	122 ± 18	117	0.6 ± 0.1	0.6	139 ± 24	130	6.4–29
	o-NH_3	I	3.7 ± 0.7	3.9	106 ± 9	104	2.3 ± 0.3	2.4	127 ± 11	126	0.1–0.2
		II	3.7 ± 0.7	3.9	106 ± 9	105	2.3 ± 0.3	2.4	128 ± 12	126	11–84
B1a	p-NH_3	I	1.6 ± 0.1	1.6	275 ± 98	211	1.3 ± 0.0	1.3	400 ± 144	319	1.1–32.2
		II	1.6 ± 0.2	1.6	182 ± 61	146	1.3 ± 0.1	1.3	243 ± 90	184	5.2–6.4
	o-NH_3	I	7.7 ± 1.5	8.1	98 ± 8	97	4.3 ± 0.7	4.4	119 ± 11	117	10.3–14.1
		II	7.8 ± 1.5	8.1	98 ± 8	97	4.3 ± 0.7	4.4	119 ± 11	117	1.7–2.8
B1b	p-NH_3	I	1.5 ± 0.1	1.6	103 ± 11	100	1.3 ± 0.0	1.3	118 ± 13	115	1.9–2.9
		II	1.6 ± 0.2	1.7	83 ± 8	82	1.3 ± 0.1	1.3	96 ± 11	96	3–98
	o-NH_3	I	4.7 ± 0.9	4.9	94 ± 7	93	2.8 ± 0.4	2.9	112 ± 9	110	1.4–4.7
		II	4.7 ± 0.9	4.9	94 ± 7	93	2.8 ± 0.4	2.9	112 ± 9	110	0.01–13
B1c	p-NH_3	I	1.7 ± 0.2	1.7	116 ± 16	112	1.4 ± 0.1	1.4	136 ± 20	131	63.1–70.4
		II	1.8 ± 0.2	1.9	87 ± 9	85	1.4 ± 0.1	1.4	102 ± 12	100	0.4–2.1
	o-NH_3	I	5.4 ± 1.0	5.6	86 ± 6	86	3.1 ± 0.5	3.1	102 ± 8	102	0.2–27.6
		II	5.4 ± 1.0	5.6	86 ± 6	86	3.1 ± 0.5	3.2	102 ± 8	101	0.1–0.2
B1i	p-NH_3	I	0.6 ± 0.1	0.7	329 ± 117	253	0.6 ± 0.1	0.6	433 ± 152	319	1.8–2.4
		II	0.7 ± 0.1	0.7	476 ± 181	92	0.6 ± 0.1	0.6	523 ± 189	92	0.01–11.2
	o-NH_3	I	1.5 ± 0.2	1.5	98 ± 7	98	1.1 ± 0.1	1.1	109 ± 7	108	38.2–42.7
		II	1.5 ± 0.2	1.5	98 ± 7	98	1.1 ± 0.1	1.1	109 ± 7	108	9–34
B2a	p-NH_3	I	3.2 ± 0.4	3.3	86 ± 8	84	2.3 ± 0.2	2.3	101 ± 10	99	1.7–23.2
		II	3.7 ± 0.4	3.8	68 ± 6	67	2.5 ± 0.2	2.5	81 ± 7	80	0.01–0.02
	o-NH_3	I	11.7 ± 2.3	12.1	83 ± 6	83	6.0 ± 1.0	6.2	100 ± 8	99	1.3–13.6
		II	11.7 ± 2.3	12.1	84 ± 6	83	6.0 ± 1.0	6.2	99 ± 7	98	0.2–10
B2b	p-NH_3	I	2.4 ± 0.2	2.4	95 ± 11	93	1.8 ± 0.1	1.8	111 ± 13	109	6.7–11.2
		II	2.7 ± 0.3	2.7	71 ± 6	71	1.9 ± 0.2	2.0	84 ± 8	83	0.01–6
	o-NH_3	I	11.9 ± 2.4	12.4	75 ± 4	75	6.1 ± 1.1	6.4	89 ± 6	88	1.1–51.0
		II	12.6 ± 2.4	12.4	75 ± 4	75	6.1 ± 1.1	6.4	89 ± 6	88	0.5–3

Notes.
[a] Estimated by excluding the (7,7) line because no collision rate is given in LAMDA.
[b] Case I corresponds to a unity filling factor for all lines at any pixel; Case II corresponds to a unity filling factor for (1,1)–(3,3) and as 0.1 for (4,4)–(7,7) at any pixel.
[c] Assuming a narrow ("n") FWHM line width of 4 km s^{-1} (the median from the fittings to the observed spectrum in Table 1).
[d] Assuming a broad ("b") FWHM line width of 9 km s^{-1} adopted from Bachiller et al. (1993) and Lefloch et al. (2012).
[e] The PDF is not obvious, so the range of the best fits based on different line width assumptions is listed.

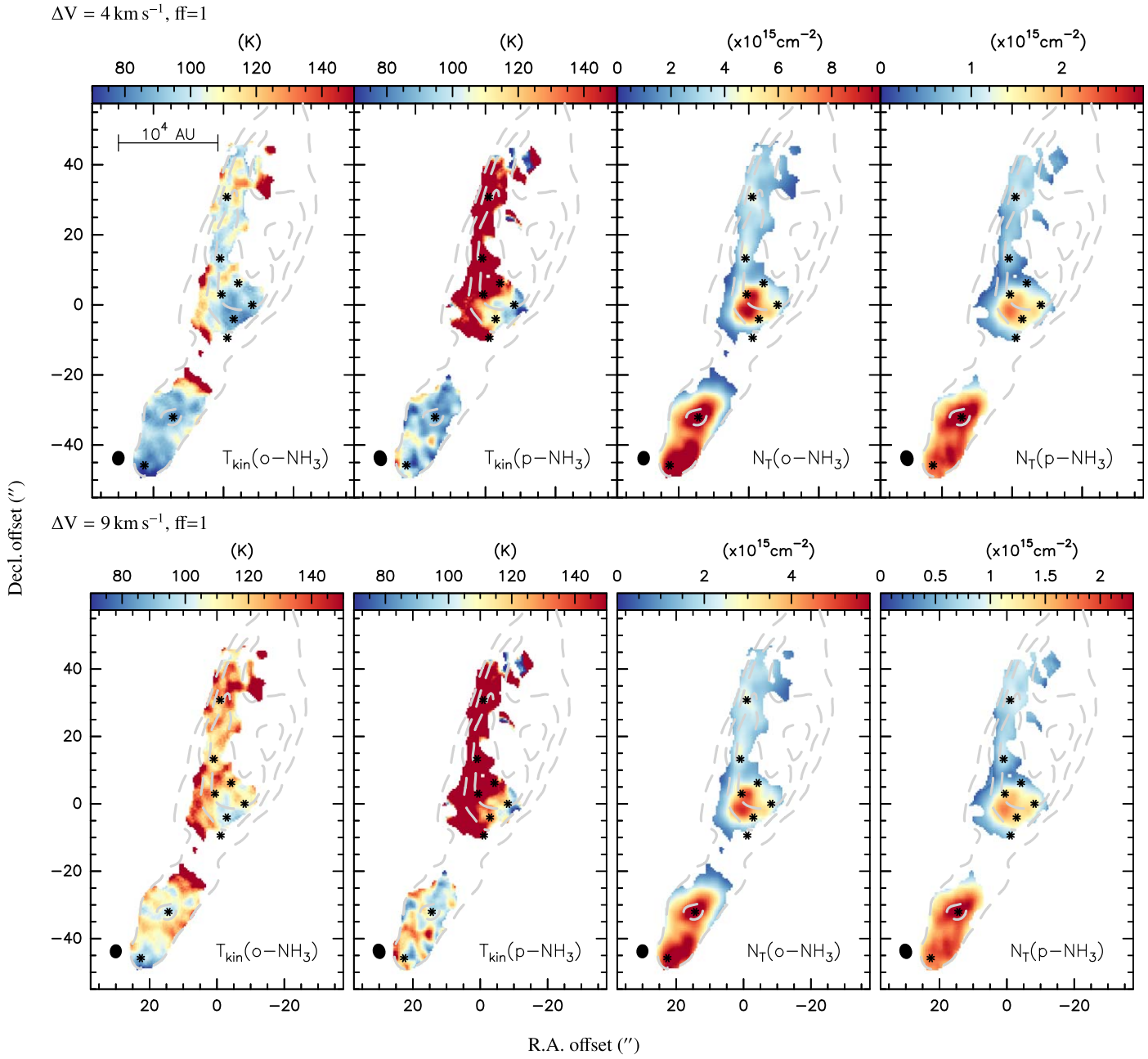

Figure D2. The best fit of the kinetic temperature maps and column density maps for *o*- and *p*-NH_3, derived from LVG MultiNest, by assuming a single component and unity filling factor for all lines toward each position. The results assuming the line width as 4 km s^{-1} and 9 km s^{-1} are shown in the upper and lower rows, respectively. The pixels where the NH_3 (5,5) and (6,6) lines show $<5\sigma$ emission and CO(1–0) show $< 8\sigma$ emission are blank for *p*- and *o*-NH_3, respectively. The gray dashed contours and the labeled clumpy substructures are the same as shown in Figure 1. These maps are derived by smoothing all lines to the same pixel size and angular resolution, i.e., $4\farcs90 \times 3\farcs81$, shown as the synthesized beam in the bottom left of each panel.

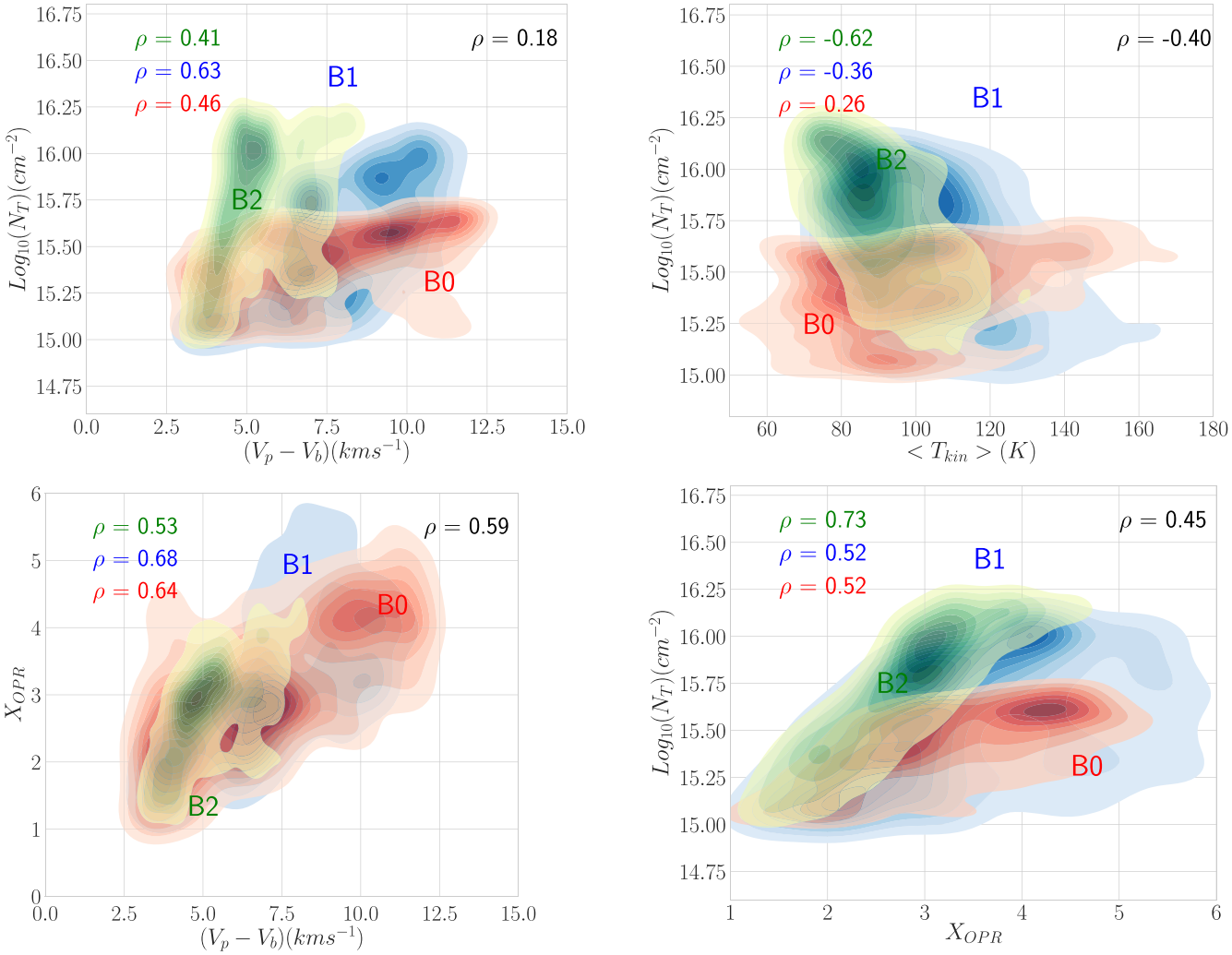

Figure D3. Possible correlation between variables. Values are extracted from pixels after smoothing the parameter maps to the same angular resolution and plotted with a bivariate Gaussian kernel density estimate as contours. B0, B1, and B2 are plotted, with the Spearman's rank correlation coefficient ρ given in red, blue, and yellowish green, respectively, while the correlation coefficient of the entire target is given in black. The pixels where the NH_3 (5,5) and (6,6) lines show $<5\sigma$ emission are blank.

satellite emission, the uncertainty for the (1,1) line is >20%. Nevertheless, it does not change our best-fit result significantly because the uncertainty for the (2,2) line is <30% and for the rest lines is <10% (less than the systematic uncertainty).

ORCID iDs

S. Feng (冯思轶) https://orcid.org/0000-0002-4707-8409
H. B. Liu https://orcid.org/0000-0003-2300-2626
P. Caselli https://orcid.org/0000-0003-1481-7911
A. Burkhardt https://orcid.org/0000-0003-0799-0927
F. Du https://orcid.org/0000-0002-7489-0179
R. Bachiller https://orcid.org/0000-0002-5331-5386
C. Codella https://orcid.org/0000-0003-1514-3074
C. Ceccarelli https://orcid.org/0000-0001-9664-6292

References

Arce, H. G., Santiago-García, J., Jørgensen, J. K., Tafalla, M., & Bachiller, R. 2008, ApJL, 681, L21
Astropy Collaboration, Robitaille, T. P., Tollerud, E. J., et al. 2013, A&A, 558, A33
Bachiller, R., Martin-Pintado, J., & Fuente, A. 1993, ApJL, 417, L45
Bachiller, R., Pérez Gutiérrez, M., Kumar, M. S. N., & Tafalla, M. 2001, A&A, 372, 899
Benedettini, M., Viti, S., Codella, C., et al. 2007, MNRAS, 381, 1127
Benedettini, M., Viti, S., Codella, C., et al. 2013, MNRAS, 436, 179
Bouhafs, N., Rist, C., Daniel, F., et al. 2017, MNRAS, 470, 2204
Burkhardt, A. M., Dollhopf, N. M., Corby, J. F., et al. 2016, ApJ, 827, 21
Busquet, G., Lefloch, B., Benedettini, M., et al. 2014, A&A, 561, A120
Caselli, P., Bizzocchi, L., Keto, E., et al. 2017, A&A, 603, L1
Ceccarelli, C., Bacmann, A., Boogert, A., et al. 2010, A&A, 521, L22
Ceccarelli, C., Caselli, P., Fontani, F., et al. 2017, ApJ, 850, 176
Chiang, H.-F., Looney, L. W., Tobin, J. J., & Hartmann, L. 2010, ApJ, 709, 470
Codella, C., Benedettini, M., Beltrán, M. T., et al. 2009, A&A, 507, L25
Codella, C., Ceccarelli, C., Bianchi, E., et al. 2020, A&A, 635, A17
Codella, C., Ceccarelli, C., Caselli, P., et al. 2017, A&A, 605, L3
Codella, C., Fontani, F., Ceccarelli, C., et al. 2015, MNRAS, 449, L11
Codella, C., Lefloch, B., Ceccarelli, C., et al. 2010, A&A, 518, L112
Cohen, J. 1988, Statistical Power Analysis for the Behavioral Sciences (London: Routledge)
Crapsi, A., Caselli, P., Walmsley, M. C., & Tafalla, M. 2007, A&A, 470, 221
Danby, G., Flower, D. R., Valiron, P., Schilke, P., & Walmsley, C. M. 1988, MNRAS, 235, 229
Downes, T. P., & Ray, T. P. 1999, A&A, 345, 977
Estalella, R. 2017, PASP, 129, 025003
Faure, A., Hily-Blant, P., Le Gal, R., Rist, C., & Pineau des Forêts, G. 2013, ApJL, 770, L2
Feng, S., Codella, C., Ceccarelli, C., et al. 2020, ApJ, 896, 37

Feroz, F., & Hobson, M. P. 2008, MNRAS, 384, 449
Feroz, F., Hobson, M. P., & Bridges, M. 2009, MNRAS, 398, 1601
Feroz, F., Hobson, M. P., Cameron, E., & Pettitt, A. N. 2019, OJAp, 2, 10
Flower, D. R., Pineau Des Forêts, G., & Walmsley, C. M. 2006, A&A, 449, 621
Fontani, F., Codella, C., Ceccarelli, C., et al. 2014a, ApJL, 788, L43
Fontani, F., Sakai, T., Furuya, K., et al. 2014b, MNRAS, 440, 448
Frank, A., Ray, T. P., Cabrit, S., et al. 2014, in Protostars and Planets VI, ed. H. Beuther et al. (Tucson, AZ: Univ. Arizona Press), 451
Ginsburg, A., & Mirocha, J. 2011, PySpecKit: Python Spectroscopic Toolkit, Astrophysics Source Code Library, ascl:1109.001
Goddi, C., Greenhill, L. J., Humphreys, E. M. L., Chandler, C. J., & Matthews, L. D. 2011, ApJL, 739, L13
Goldreich, P., & Scoville, N. 1976, ApJ, 205, 144
Gómez-Ruiz, A. I., Codella, C., Lefloch, B., et al. 2015, MNRAS, 446, 3346
Gómez-Ruiz, A. I., Hirano, N., Leurini, S., & Liu, S.-Y. 2013, A&A, 558, A94
Gueth, F., Guilloteau, S., & Bachiller, R. 1996, A&A, 307, 891
Gueth, F., Guilloteau, S., & Bachiller, R. 1998, A&A, 333, 287
Harju, J., Daniel, F., Sipilä, O., et al. 2017, A&A, 600, A61
Ho, P. T. P., & Townes, C. H. 1983, ARA&A, 21, 239
Juvela, M., & Ysard, N. 2011, ApJ, 739, 63
Lee, K., Looney, L., Johnstone, D., & Tobin, J. 2012, ApJ, 761, 171
Lefloch, B., Bachiller, R., Ceccarelli, C., et al. 2018, MNRAS, 477, 4792
Lefloch, B., Cabrit, S., Busquet, G., et al. 2012, ApJL, 757, L25
Lefloch, B., Cabrit, S., Codella, C., et al. 2010, A&A, 518, L113
Lefloch, B., Ceccarelli, C., Codella, C., et al. 2017, MNRAS, 469, L73
Looney, L. W., Tobin, J. J., & Kwon, W. 2007, ApJL, 670, L131
Mangum, J. G., & Shirley, Y. L. 2015, PASP, 127, 266
McMullin, J. P., Waters, B., Schiebel, D., Young, W., & Golap, K. 2007, in ASP Conf. Ser. 376, Astronomical Data Analysis Software and Systems XVI, ed. R. A. Shaw, F. Hill, & D. J. Bell (San Francisco, CA: ASP), 127
Neufeld, D. A., DeWitt, C., Lesaffre, P., et al. 2019, ApJL, 878, L18
Offer, A., & Flower, D. R. 1989, JPhB, 22, L439
Perley, R. A., & Butler, B. J. 2017, ApJS, 230, 7
Pety, J. 2005, in SF2A-2005: Semaine de l'Astrophysique Francaise, ed. F. Casoli (Les Ulis: EdP-Sciences), 721
Podio, L., Codella, C., Gueth, F., et al. 2016, A&A, 593, L4
Podio, L., Lefloch, B., Ceccarelli, C., Codella, C., & Bachiller, R. 2014, A&A, 565, A64
Rist, C., Alexander, M. H., & Valiron, P. 1993, JChPh, 98, 4662
Rosolowsky, E. W., Pineda, J. E., Foster, J. B., et al. 2008, ApJS, 175, 509
Schöier, F. L., van der Tak, F. F. S., van Dishoeck, E. F., & Black, J. H. 2005, A&A, 432, 369
Shirley, Y. L. 2015, PASP, 127, 299
Smith, M. D., Suttner, G., & Yorke, H. W. 1997, A&A, 323, 223
Sobolev, V. V. 1960, Moving Envelopes of Stars (Cambridge, MA: Harvard Univ. Press)
Spezzano, S., Codella, C., Podio, L., et al. 2020, A&A, 640, A74
Tafalla, M., & Bachiller, R. 1995, ApJL, 443, L37
Teague, R., & Foreman-Mackey, D. 2018, RNAAS, 2, 173
Tobin, J. J., Cox, E. G., & Looney, L. W. 2022, ApJ, 928, 61
Tobin, J. J., Hartmann, L., Looney, L. W., & Chiang, H.-F. 2010, ApJ, 712, 1010
Umemoto, T., Mikami, H., Yamamoto, S., & Hirano, N. 1999, ApJL, 525, L105
van der Tak, F. F. S., Black, J. H., Schöier, F. L., Jansen, D. J., & van Dishoeck, E. F. 2007, A&A, 468, 627
van der Walt, S., Colbert, S. C., & Varoquaux, G. 2011, CSE, 13, 22
Viti, S., Jimenez-Serra, I., Yates, J. A., et al. 2011, ApJL, 740, L3
Walmsley, C. M., & Ungerechts, H. 1983, A&A, 122, 164
Zhang, Q., Ho, P. T. P., & Wright, M. C. H. 2000, AJ, 119, 1345
Zucker, C., Speagle, J. S., Schlafly, E. F., et al. 2019, ApJ, 879, 125